



REGULAR PAPER

Zhanwei Hu · Jinsheng Liu · Lian Gan · Shengjin Xu

## Wake modes behind a streamwisely oscillating cylinder at constant and ramping frequencies

Received: 12 August 2018 / Revised: 23 December 2018 / Accepted: 23 December 2018 / Published online: 25 March 2019  
© The Author(s) 2019

**Abstract** In this paper, the wake modes behind a circular cylinder under streamwisely forcing oscillating motion are studied at Reynolds number  $Re = 360\text{--}460$  which are observed by laser-induced fluorescence flow visualization technique. The forcing frequency  $f_e$  ranges from 0 to  $6.85 f_s$ , where  $f_s$  is the vortex shedding frequency behind a stationary cylinder, and the forcing amplitude  $A/d = 0.2, 0.5, 1.0$ , where  $d$  is the cylinder diameter. Both time-invariant and linearly ramping  $f_e$  are investigated. Following our previous modal notation, the following conclusions can be drawn: firstly, three rarely reported modes in numerical studies, C-I, C-II and S-III, are now confirmed in experiments (though with differentiable appearance in their far wake behaviour) at higher  $A$  and/or  $f_e$  ranges and the envelope lines of S modes and C modes, yielded from a vortex circulation model, are shown to be dependent on the peak relative velocity of the free stream to the cylinder surface. So is the occurrence of the S-II mode. Secondly, near the demarcation of A modes and S-I mode, wake mode undergoes constant transition in a stochastic manner at fixed  $Re$ ,  $A$  and  $f_e$ . Thirdly, a typical hysteretic effect can be observed when the oscillation frequency of the cylinder ramps up and down in a linear way, and the extent of delay is dependent on the ramping rate  $k$ . Finally, mode switching during frequency ramping obeys a unidirectional order. During  $k < 0$  (ramp-down), when S-I (Type-II) mode switches to A-IV mode, or A-IV to A-III, the flow structure downstream is affected by the upstream and the entire wake flow eventually switched, which is classified as slow switches. In contrast, during  $k > 0$  (ramp-up), a clear and abrupt switch can be observed in the wake when A-IV or A-III switch to S-I (Type-II) modes, which are jump switches.

**Keywords** Streamwise oscillation · Vortex shedding · Wake

### List of symbols

$A$  Forcing amplitude  
 $l$  Spanwise length of the cylinder  
 $d$  Cylinder diameter

---

Z. Hu · J. Liu · S. Xu (✉)  
AML, School of Aerospace Engineering, Tsinghua University, Zhongguancun North Street, Haidian District,  
Beijing 100084, China  
E-mail: xu\_shengjin@tsinghua.edu.cn  
Tel.: +86 10 62788941

L. Gan (✉)  
Department of Engineering, Durham University, Durham DH1 3LE, UK  
E-mail: lian.gan@durham.ac.uk

Z. Hu  
China Aerodynamics Research and Development Centre, Mianyang, China

$U_0$	Free stream velocity
$\nu$	Kinematic viscosity of the working fluid
$Re$	Reynolds number based on the free stream velocity $Re = U_0 d / \nu$ .
$f_e$	Fixed forcing frequency of cylinder
$t$	Time
$k$	Ramping rate
$\phi_0$	Arbitrary starting phase
$v_c$	Linear velocity of the oscillating cylinder $v_c = 2\pi A f_e \sin(2\pi f_e t + \phi_0)$
$f_s$	Vortex shedding frequency behind a stationary cylinder
$St$	Strouhal number $St = f_s U_0 / d$
$X(t)$	Motion displacement $X(t) = A \cos(2\pi f_e t + \phi_0)$
$x$	Streamwise direction
$y$	Transverse direction
$\Gamma$	Circulation of individual vortex packet
$f(C-I)$	Frequency of vortex shedding of C-I mode at $x \approx 4d$
$Re_c$	Critical Reynolds number for the formation of S-II mode
$V_i$	Induced velocity
$Re_p$	Peak (relative) Reynolds number $Re_p = 2\pi f_e A D / \nu + Re$
$\Delta Re$	Relative Reynolds number $\Delta Re = (2\pi f_e A - U_0) D / \nu$
$\Gamma_{cp}$	Circulation of the vortices formed by the $+x$ relative velocity
$Re_{cp}$	Circulation-based Reynolds number: $Re_{cp} = \Gamma_{cp} / \nu$
$N$	Number of oscillation cycles spent in change from one frequency ramping to another
$N_{rp}$	Number of cycles of the entire ramp-up/down period.

## 1 Introduction

The wake flow behind a circular cylinder under sinusoidal oscillation motion in streamwise direction is of both fundamental and practical relevance. The oscillation motion relative to the incoming flow can be generated not only by the motion on the cylinder itself, but also by an unsteady periodic perturbation superimposed on the uniform free stream and impact on a stationary cylinder. Oil or gas platform riser cables and the bridge piers are sample cylindrical-shaped structures exposed to ocean currents or winds, which are often highly unsteady in the form of waves of various wavelengths. Compared with classical Karman vortex street behind a stationary cylinder in a steady uniform in coming flow, if vibrations induced by the periodic incoming flow occur on flexibly mounted cylinders, which can be in both streamwise and transverse direction, the vortex shedding behaviour will become significantly complex, due to the combination of the unsteady motions on both the incoming flow and the structure. It may cause drag and lift on the structure to change rapidly and also those on the downstream one, which further induces fluttering or galloping and hence structural fatigue damage. While wake behind a cylinder under transverse vibration motion, either induced or forced, has been studied extensively (e.g. Williamson and Govardhan 2004; Williamson and Roshko 1988), wake pattern behind a cylinder under streamwise oscillation motion has attracted less attention, which, however, is equally important to problems like flow-induced vibration and flow control (Naudascher 1987; Sarpkaya 2004).

If the incoming flow is uniform and steady, at the right condition, transverse oscillation will occur spontaneously on the cylinder, induced by the alternative vortex shedding, while streamwise oscillation usually requires external forcing to result in a reasonable amplitude, i.e. according to Konstantinidis (2014) and Konstantinidis and Bouris (2016), the amplitude of a spontaneous streamwise oscillation is typically smaller than  $0.15d$ , where  $d$  is the cylinder diameter. In such a flow condition, in addition to Reynolds number,  $Re = U_0 d / \nu$ , where  $U_0$  is the free stream velocity and  $\nu$  is the kinematic viscosity of the working fluid, the flow is further controlled by the frequency of the external oscillatory driving force,  $f_e$  and the amplitude  $A$ . In dimensionless forms, the two governing parameters are  $A / d$  and the frequency ratio  $f_e / f_s$ , where  $f_s$  is the vortex shedding frequency from a stationary cylinder under the same  $Re$ .

Tanida et al. (1973) measured lift and drag forces on a streamwisely oscillating circular cylinder to study the stability of the oscillation motion at  $A/d = 0.14$  and  $f_e/f_s = 0-2.0$ . They found that the streamwise oscillation causes the so-called synchronization in a range around double the Strouhal frequency, viz  $f_e/f_s = 0.77-1.54$  ( $Re = 80$ ). They thought that the fluctuating forces consist of two parts: one is due to the vortex shedding, and the other is resulted from the cylinder oscillation. Griffin and Ramberg (1976)

visualized the vortex formation from a circular cylinder oscillating in line with the incoming flow at  $Re = 190$ . They found that the vortex shedding is all in the ‘lock-on’ condition, where the vortex shedding frequency coincides with that of the structural oscillation frequency and near twice the Strouhal frequency, i.e. in the range of  $f_e/f_s = 1.74\text{--}2.2$  and  $A/d = 0.06\text{--}0.12$ . Two distinct wake patterns (A-I and A-III) are also reported for the first time. Ongoren and Rockwell (1988a, b) investigated the wake pattern when  $A/d = 0.13$  and  $0.3, 0.5 < f_e/f_s < 4.0$ . They identified two basic modes, which are the symmetric and anti-symmetric vortex formation, and further classified these two basic modes to five submodes: S mode for the symmetric vortex formation and A-I, II, III, IV modes for the anti-symmetric vortex formation. Cetiner and Rockwell (2001) studied the lock-on state of a streamwisely oscillating circular cylinder in a cross flow ( $0.3 < f_e/f_s < 3.0$ ) and found that the time-dependent transverse force was phase-locked to the circular cylinder motion and the vortex system appeared at both upstream and downstream of the cylinder.

Detemple-Laake and Eckelmann (1989) carried out smoke-wire flow visualization of the wake patterns in a sinusoidally sound superimposed open-circuit wind tunnel at  $Re = 60\text{--}200$ . Three types of lock-on modes of wake patterns, with rich details in both streamwise and spanwise directions, were presented and discussed with limit cycles. Nishihara et al. (2005) measured the fluid forces acting on a cylinder forced to oscillate in the streamwise direction and showed the corresponding detailed flow visualization of the wake patterns at  $A/d = 0.05$  for a range of reduced velocities in a water tunnel at subcritical Reynolds numbers. They illustrated the relationship between the damping coefficients and the wake patterns.

Xu (2003) and Xu et al. (2006) increased the oscillation amplitude from  $A/d = 0.5\text{--}0.67$  and found the S-II mode, which consists of two rows of binary vortices symmetrically arranged about the wake centreline. By decomposing the vorticity production into two components that associated with the oscillation of a cylinder in quiescent fluid and that associated with the flow past a stationary cylinder, they concluded that the critical  $A/d$  at which the S-II mode occurs scales with  $(f_e/f_s)^{-1}$ . Konstantinidis and Balabani (2007) found that S-II mode could rapidly break down and give rise to an anti-symmetric arrangement of vortex structures further downstream. The downstream wake may or may not be phase-locked to the imposed oscillation.

In addition to the experiments, some numerical simulations have also been applied to investigate similar problems, which enriched dynamic data for the wake mode structures. For example, Song and Song (2003) suggested that the primary and the secondary vortices of S mode are generated by the instability of the vortex sheet and the forcing motion on the cylinder, respectively. Yufei et al. (2007) performed a detailed investigation in lock-on region and proposed  $Af_e^2/df_s^2$  to be an important control parameter for different vortex shedding modes, which successfully predicts the symmetric S mode. Leontini et al. (2013) examined the impact on the vortex shedding frequency of  $A$  and  $f_e$  of the oscillation, as well as  $Re$  of the incoming flow. The observed declined rates of the frequency with respect to  $A$  are shown to be able to predict the oscillation amplitude  $A$  on the cylinder when synchronization occurs. Zhou and Graham (2000) computationally studied cylinder placed in oscillatory currents and observed vortex pattern in the wake similar to the experimental visualization by Couder and Basdevant (1986). However, differences in the far-field dissipation of vortex were noticed. Sarpkaya et al. (1992) carried out numerical simulations in so-called laminar pulsatile flows and revealed that wake comprises of three rows of heterostrophic vortices certain oscillation conditions.

Summarizing these previous studies, in which the maximum oscillation amplitude  $(A/d)_{\max} < 0.8$  and the maximum forcing frequency  $(f_e/f_s)_{\max} < 3$ , six wake modes have been identified behind a streamwisely oscillating cylinder, namely the anti-symmetric A-I, II, III, IV modes and the symmetric S-I, II modes. Moreover, the above-mentioned works were conducted under time-invariant  $f_e$  exclusively. The present work aims to explore possible new wake modes at a higher  $A/d$  and  $f_e/f_s$  range and provide empirical model for their envelope lines. Moreover, the transient mode switching under the effect of continuous time-variant forcing frequencies, which is more likely to occur in the real world unsteady flow conditions, is investigated for the first time, to the best of the authors’ knowledge.

## 2 Experimental details

Laser-induced fluorescence (LIF) technique was employed to visualize the wake modes. The LIF measurement was carried out in a closed-loop water channel, which has a square working section ( $0.5\text{ m} \times 0.5\text{ m}$ ) of  $3\text{ m}$  long. The speed of the water flow  $U_0$  is controlled by an AC frequency converter. The maximum  $U_0$  obtained in the working section is about  $0.5\text{ m/s}$ , with the maximum free stream

turbulence intensity about 0.2%. A circular cylinder made of stainless steel with diameter  $d = 12$  mm and spanwise length  $l = 360$  mm was vertically mounted at the middle of the working section. The top end of the cylinder was attached to an actuator. The linear oscillation motion of the actuator is driven by a DC servo motor with an in-line slider-crank mechanism along a pair of linear guide rails, which can be accurately controlled by programming a microcomputer, with 8-bit resolution. A laser levelling gage was used to calibrate the perpendicularity of the cylinder. A high-speed camera with  $\approx 40 \mu\text{m}/\text{pixel}$  resolution (after calibration) was used to track and validate the cylinder motion, in order to reassure the motion accuracy. A flat plate about  $0.5 \text{ m} \times 0.5 \text{ m}$  in size, with a slot cut to allow the cylinder go through, was placed about 3 mm under the free surface of water to suppress surface wave and ripple when the cylinder is in oscillation motion.

A simple sinusoidal oscillating motion in the streamwise direction was forced on the cylinder. The motion displacement  $X(t)$  can be written as

$$X(t) = A \cos(2\pi f_e t + \phi_0), \quad (1)$$

where the oscillation amplitude  $A$  applied in this study are  $0.2d$ ,  $0.5d$  and  $1.0d$ ,  $f_e$  which ranges 0–3.5 Hz, corresponds to  $0\text{--}6.85f_s$  ( $f_s = StU_0/d$ , where  $St$  is the Strouhal number obtained behind a stationary cylinder),  $\phi_0$  is the arbitrary starting phase. In the present study,  $f_e$  ramps up from and down to zero in a linear manner. As a function of time, it can be expressed as

$$f_e(t) = f_0 + kt, \quad (2)$$

where  $f_0 = 0\text{Hz}$  and  $|k| = 0.02, 0.04, 0.08, 0.14, 0.22, 0.44$  ( $\text{s}^{-2}$ ) and  $t(\text{s})$  is real time. In the fixed  $f_e$  cases ( $f_0 = f_e$  and  $k = 0$ ). In total 30 s of constant frequency duration is ensured, i.e. modes are recorded after they are sufficiently stabilized.

The measurements are performed on the central section of the test cylinder, so as to minimize three-dimensional flow effects. Rhodamine Dye (6G 99%), which turns metallic green colour when excited by a laser of 532 nm wavelength, was introduced at the mid-span through two injection pinholes located at  $\pm 90^\circ$  on the cylinder surface (the leeward stagnation point being  $0^\circ$ ), as shown in Fig. 1. With a valve controlling the flow rate, dye came out from the pinholes by the hydraulic head created by a dye reservoir, which was placed about 0.8 m above the free water surface in the channel. The head was carefully adjusted to compromise the injection momentum, which is negligible compared to the free stream momentum but is enough to create a flow rate which sufficiently contrasts the subtle wake structures from the background flow. The size of the pinholes is about 0.15 mm in diameter. The near-field wake region was illuminated by a thin sheet of about 2 mm thick emitted from a 10 W continuous wave laser. The field of view (FOV) is about  $-1 \leq x/d \leq 15$  and  $-4 \leq y/d \leq 4$  in the streamwise and spanwise directions, respectively, where  $(x, y) = (0, 0)$  is at the cylinder centre. A professional digital video camcorder (SONY PXW-X280) was used to record the wake flow at 25 frames per second (fps). Measurements were conducted at  $Re = 360\text{--}460$ .

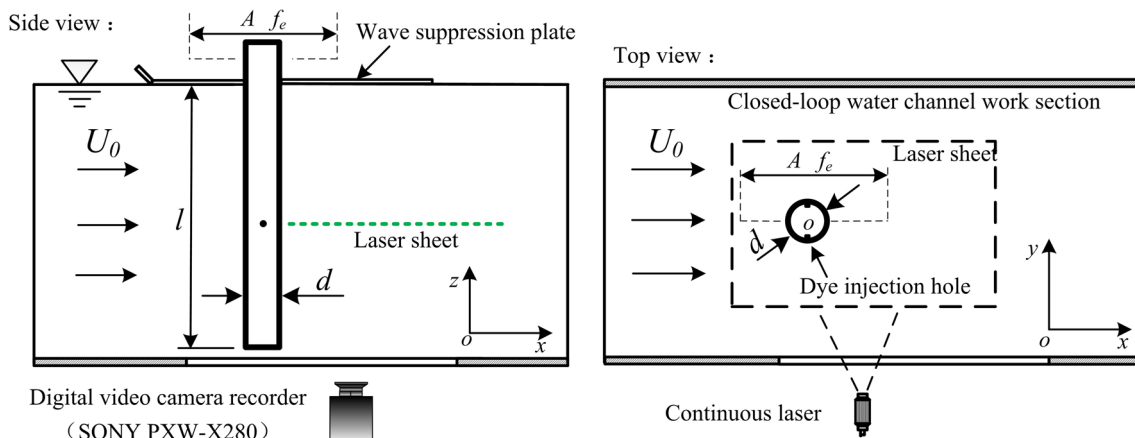


Fig. 1 Experimental set-up, sketch is not to scale

### 3 Wake modes induced by constant $f_e$

In the lock-on regime, the wake mode behind a streamwisely oscillating cylinder depends on the combination of  $A/d$  and  $f_e/f_s$ . The present LIF visualization confirms the occurrence of five basic modes reported previously, albeit at different  $A/d, f_e/f_s$  combinations. The conditions for the occurrence of these modes in the present study are given in Sect. 3.3.

We also observed three modes which have not been discussed well previously, to the best of our knowledge. They typically occur at high  $A/d$  and/or  $f_e/f_s$  ranges, which are denoted as S-III, C-I and C-II modes. These modes are schematically described in Fig. 2, together with the terminology of other modes. It is worth mentioning that S-III mode is similar to the vortex pattern observed by Sarpkaya et al. (1992) numerically. Nevertheless, the formation process was not discussed in detail and the far-field wake seems to have higher viscous effect, even at higher  $Re$ , which might be owing to the forced two-dimensional condition in the simulation (while three-dimensional effect is inevitable in experiments), especially in the far field. Moreover, in our experiments, we also observe two submodes of S-III, and their formation conditions will be briefly discussed next.

At  $f_e/f_s > 4.5$  and  $A/d = 0.2$ , the near-field wake displays two rows of small size vortices symmetrically aligned about the wake centreline, which are originated from the shear layer roll-up. By  $x \approx 4d$  downstream, the classical alternative Karman vortex street is recovered. This mode is referred to as the C-I mode shown in Fig. 2. At the same frequency, as  $A$  increases to  $0.5d$ , shear layer vortices recovering to Karman vortex street cannot be achieved; instead, the wake quickly becomes chaotic by  $x \approx 1d$ . This mode is denoted as the C-II mode and is shown in Fig. 2. Interestingly, when a subtle reduction of  $f_e$  is applied (at the same  $A$ ), the chaotic wake pattern manages to quickly reorganize itself, with a binary vortex pair aligning along the centreline and another two rows of binary vortex pair emerging symmetrically in the outer flow, on both sides of the wake centreline. This mode, with the additional vortex pair rolled up at the wake centreline, is mode S-III, similar to that depicted in Sarpkaya et al. (1992). Depending on whether the outer vortex pairs manage to turn their way towards the centreline before broken, this mode can be further categorized to Type-I and Type-II modes as shown in Fig. 2.

#### 3.1 C-I and C-II modes

Figure 3 presents a schematic drawing of the C-I mode formation process. During each oscillation period ( $1/f_e$ ), at the motion phase where the cylinder moves upstream relative to  $U_0$ , one small pair of counter-rotating vortices forms, one on the each side of the centreline. The pair convects downstream as new pairs form during the subsequent oscillation cycles, producing a pair of vortex sheets. The formation of the small-scale vortices in the sheets is locked on to  $f_e$ . These small vortices are originated from the shear layer between the cylinder surface and the outer free stream and are labelled as  $a_n$  (negative sensed rotation) and  $b_n$ , (positive sensed)  $n = 1, 2$ . The two vortex rows lose their stability quickly and start to interact at  $x \approx 4d$  and eventually coalesce to form vortices of larger scale. The formation of these large vortices is in alternative manner as indicated by the vortices labelled as  $\Gamma_1$  and  $\Gamma_2$  in Fig. 3 which is similar to the Karman vortex street, as if the vortices are shed from a stationary cylinder but with perceptible differences. The formation of the alternative large vortices from symmetric vortex sheets is similar to the transformation from ‘Bloor–Gerrard’ vortices to alternative mode reported in Konstantinidis and Balabani (2007).

Sequential photographs of C-I formation and an example of the classical Karman vortex street in the case of  $f_e = 0$  Hz at the same  $Re$  are illustrated in Figs. 4 and 5, respectively. Compared to the shear layers in the near wake of a stationary cylinder in Fig. 5, which is clean and smooth, the vortex rows  $a_n, b_n$  behind the oscillating cylinder in Fig. 4 can be understood as shear layer instability amplified by the energy input from the small amplitude but large frequency forcing on the cylinder. The amplified instability does not appear to significantly accelerate the rolling-up of Karman type vortices, which occurs at a similar downstream location. However, it induces noticeable differences further downstream. While the trajectories of the Karman vortices behind the stationary cylinder (Fig. 5) are shown to be close to the centreline of the wake, those in Fig. 4 are displaced further apart, as indicated by the dashed lines  $L_1$  and  $L_2$ , which approximately go through the vortex centres.

The frequency of vortex shedding at  $x > 4d$  in Fig. 4, at the given  $Re$ , is found to be  $f(\text{C-I}) = 0.4883$  Hz, which is appreciably smaller than the Karman shedding frequency  $f_s = 0.537$  Hz, i.e.  $f(\text{C-I})/f_s = 0.91$  or  $f(\text{C-I})/f_e = 0.13$ . The frequency  $f(\text{C-I})$  is found to be consistently smaller than  $f_s$  at other  $Re$  and  $f_e$  conditions.

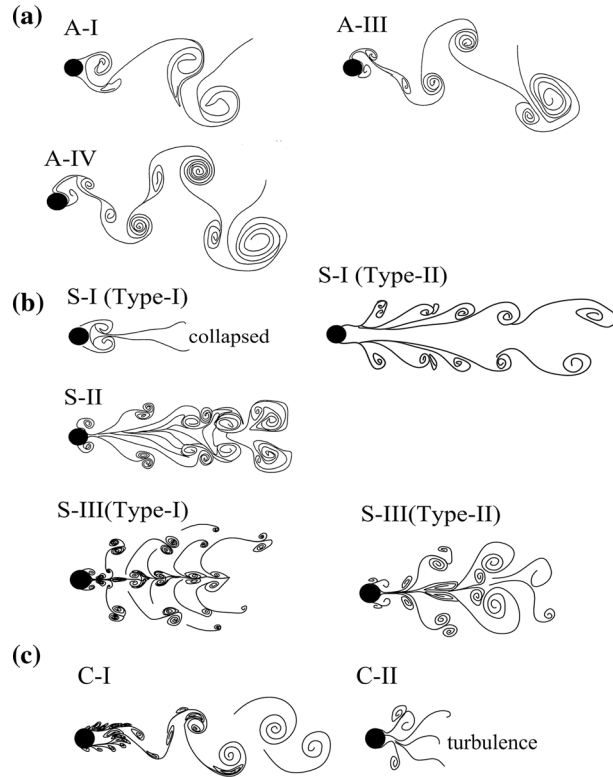


**Fig. 2** Typical flow modes reported in Xu et al. (2006) and observed in the present experiment. **a** Asymmetric modes, **b** symmetric modes, **C** Chaotic modes

These are listed in Table 1, which suggests that as  $Re$  or  $f_c/f_s$  increases, the ratio  $f(C-I)/f_s$  also increases. Therefore, C-I is a mode that is locked on in the near field but non-locked on in the far field.

The vortex shedding frequency in the wake is quantified by the temporal dependence of dye intensity. Taking the classical Karman shedding shown in Fig. 5 as example, a duration of 28 sec at 25 fps is taken and converted to 700 TIFF images. Downsampling the raw image ( $1920 \times 1080$  pixels) to  $300 \times 169$  pixels, the variation of the fine details in the raw images, as well as the computational effort are both significantly reduced. The standard snapshot-based proper orthogonal decomposition (POD) (Zhang et al. 2014; Sieber et al. 2016) is then applied to the subdomain of the images shown in Fig. 6a. The time function of the

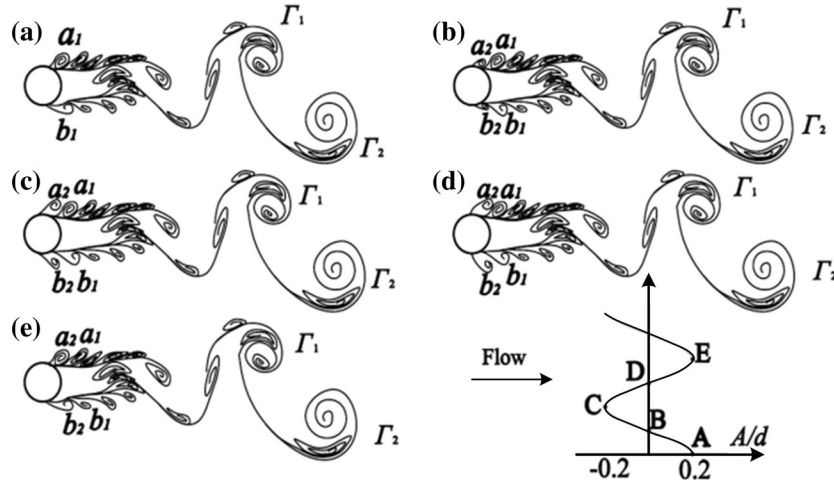


**Fig. 3** Formation process of C-I mode for a complete cylinder oscillation cycle.  $A/d = 0.2$ ,  $f_c/f_s = 6.85$  and  $Re = 360$

coefficient of Mode 1 (Mode 0 being the mean)  $a_1$  is given in Fig. 6b and its frequency spectrum using Welch algorithm (256 sample segment length and 25% overlap) is displayed in Fig. 6c, which suggests a single energetic shedding frequency in the domain. To reassure the finding, the intensity (I) variation at a single testing point, a so-called intensity probe, is investigated, which is shown in Fig. 6b. The frequency spectrum of the signal from FFT, as shown in Fig. 6c, also indicates a single peak at the same frequency. In a similar way,  $f(C-I)$  is found through POD, for the subdomain where the alternative shedding is seen, viz.  $x \leq 4d$ . Note that both POD and single point spectrum analyses are performed based on the scalar intensity, not velocity. Due to the inhomogeneous dye distribution (with gaps), which is inevitable in experiment, spectrum contains noise and should not be equivalent to the velocity spectrum. However, only the peak frequency is of interest here, which evidently has been determined with sufficient confidence.

As the forcing amplitude increases to  $A/d = 0.5$ , no clear vortex rows  $a_n b_n$  can sustain, nor can the shear layer roll up to larger vortices of Karman type. The wake quickly becomes turbulent where no coherent structure can be identified except random small-scale eddies. This mode is named C-II, which is ‘observed’ in a similar flow condition of the ‘chaos’ mode discussed in Leontini et al. (2013), since it is reasonable to deduced that a chaotic lift should be a result of a turbulent vortex shedding process without coherent patterns, as suggested in Fig. 7. Note that  $f_e = 3.86f_s$  is the highest forcing frequency that can be applied at  $A/d = 0.5$ , due to hardware limitation.

### 3.2 S-III mode

At the same amplitude ( $A/d = 0.5$ ) and  $Re = 360$ , as the forcing frequency decreases to the range  $3.0 \leq f_e/f_s \leq 3.5$ , organized wake pattern emerges in a symmetric manner about the wake centreline, as sketched in Fig. 2 and visualized in Fig. 8. Compared to the S-II mode, which is the symmetric binary vortex street observed in Xu et al. (2006), a row of counter-rotating vortices appear along the wake centreline, which are originated from the cylinder oscillation. In order to highlight the additional feature along the centreline, this mode is named S-III mode. Figure 8 presents a scenario in which the outer vortex pair (A, C) moves further away from the centreline, leaving the vortex pair (E, F) along the wake centreline undisturbed. On the contrary, in Fig. 9 when  $Re$  increases to 430, the vortex pair (A, C) moves inwards to the centreline soon after it forms, which quickly interacts with the vortex pair (E, F) to form a larger vortex pair at the centreline. Although the wake pattern looks quite different between Figs. 8 and 9, the formation processes are identical. Hence, they are categorized as submode Type-I and II of S-III, respectively. Like S-II, S-III is also a lock-on mode.

Figure 10 illustrates the S-III mode formation process during one forcing cycle. As the cylinder moves upstream ( $-x$  direction,  $t_0 \leq t \leq t_2$ ), when  $dx/dt < 0$ , the fluid near the cylinder surface is brought to move along due to no-slip condition. According to Eq. (1), the velocity of the free stream flow  $U_0$  relative to the cylinder surface will be  $U_0 + 2\pi f_e A \sin(2\pi f_e t + \phi_0)$ , where  $0 \leq (2\pi f_e t + \phi_0) \leq \pi$  during which one vortex pair A (clockwise rotating) and B (anti-clockwise) rolls up from the shear layer. The velocity induced at the centres of (A, B) from each other,  $V_i$ , according to Biot–Savart Law, is in  $-x$  direction and  $|V_i| \propto \Gamma_{A,B}$ , where  $\Gamma$  is the circulation of A or B. Initially when  $\Gamma$  is small,  $|V_i| \approx 0$  and (A, B) moves according to the

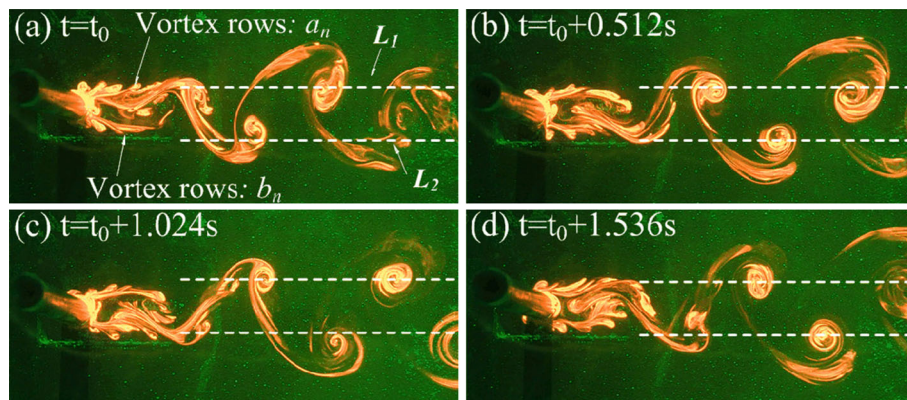


**Fig. 4** Sequential photographs of C-I mode at  $A/d = 0.2$ ,  $f_e/f_s = 6.85$  and  $Re = 360$ . **a**  $t = t_0$ , **b**  $t = t_0 + \Delta t$ , **c**  $t = t_0 + 2 \Delta t$ , **d**  $t = t_0 + 3 \Delta t$ , with  $\Delta t = 0.52s$ , where  $\Delta t^{-1} \approx 4f(C-I)$

**Table 1** Frequency of the reorganized C-I mode at  $A/d = 0.2$

$Re$	$f_e/f_s$	$f(C-I)/f_s$	$f(C-I)/f_e$
360	5.29	0.787	0.149
360	6.18	0.787	0.128
360	6.85	0.91	0.132
430	4.98	0.85	0.171
430	5.97	0.90	0.151
460	4.60	0.93	0.201

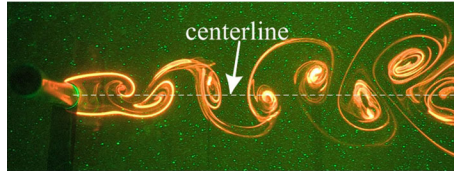


**Fig. 5** Karman vortex street behind the stationary cylinder at  $Re = 360$

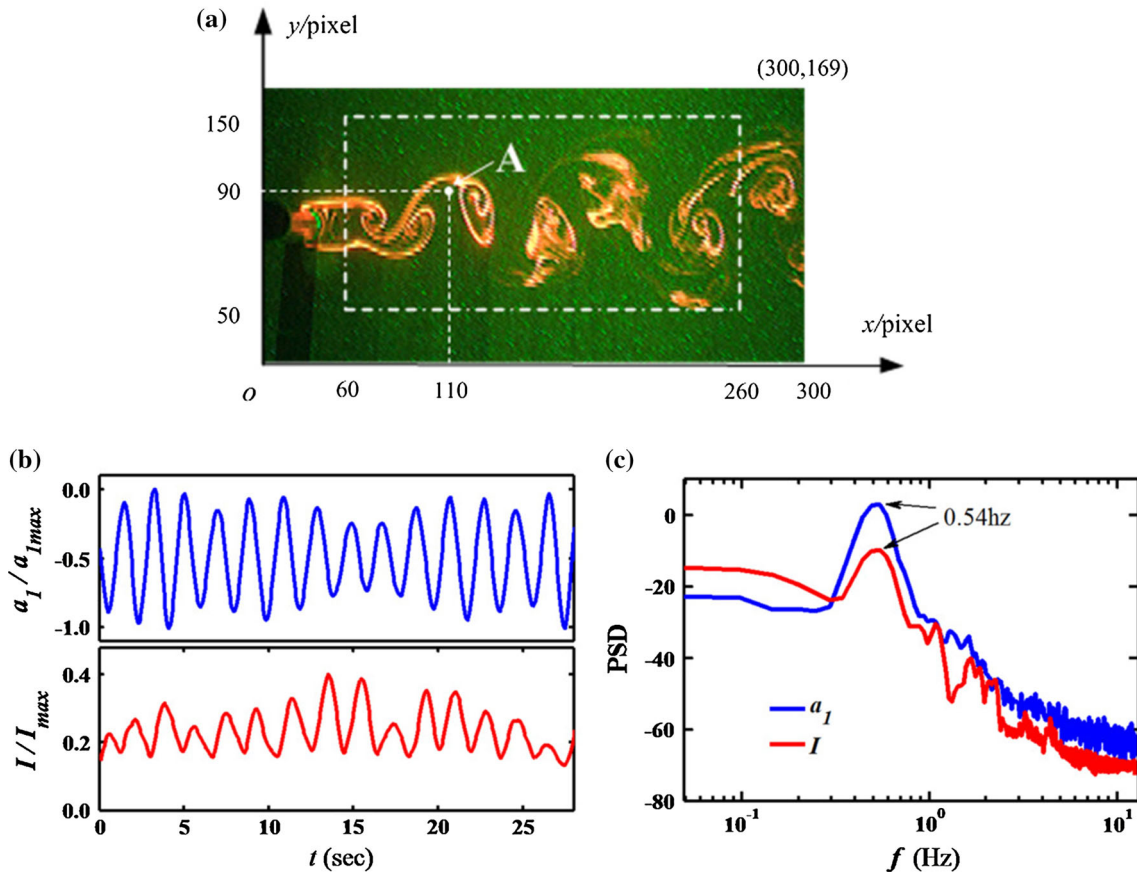


**Fig. 6** **a** Downsampled instantaneous image from the case stationary cylinder at  $Re = 360$ . Also shown are the POD examination subdomain [60:260, 50:150] and the location of the intensity probe A, at [110,90]. **b** Temporal variation of the first POD mode coefficient  $a_1$  and the intensity at the probe,  $I$ . **c** PSD of  $a_1$  and  $I$

local velocity in the shear layer. During  $t_0 \sim t_1$ , the motion of (A, B) is in the  $-x$  direction but the magnitude is smaller than that of the cylinder, and hence, (A, B) is moving away from the latter. During  $t_1 \sim t_2$ , as  $\Gamma_{A,B}$  grows,  $|V_i|$  increases, but the upstream motion of the cylinder slows down. As a result, (A, B) still moves in  $-x$  direction, but their distance to the cylinder reduces.



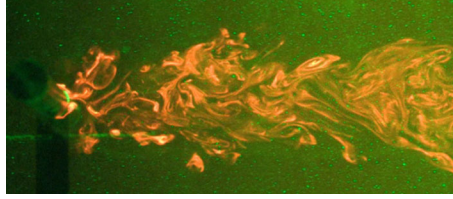


**Fig. 7** Sequential photographs of C-II mode at  $A/d = 0.5$ ,  $f_c/f_s = 3.86$  and  $Re = 430$

As the cylinder moves in the downstream (+ $x$ ) direction, viz..  $t_2 \leq t \leq t_4$ , the mean velocity of the cylinder is

$$\bar{v}_c = \frac{1}{t_4 - t_2} \int_{t_2}^{t_4} v_c(t) dt = \frac{1}{\pi} \int_0^\pi 2\pi f_c A \sin \theta d\theta, \quad (3)$$

where  $\theta = 2\pi f_c t + \phi_0$ . For the case shown here,  $f_c = 1.53$  Hz and  $\bar{v}_c = 3.68$  cm/s  $> U_0$  (3.1 cm/s). Thus, on the mean, the free stream has a velocity in  $-x$  direction relative to the cylinder surface and vortex pair (C, D) forms. Up to this moment, it follows the same formation process as S-II mode.

However, when the strength and the duration of the relative motion of the flow to the cylinder surface (in  $-x$  direction) are large enough, the shear layer induced by such a relative motion is not able to fully entrained into the vortex pair (C, D) for it to continue growing; instead, (C,D) will move along with (A, B) under the influence of the latter and the residual shear layer will roll up to a new vortex pair (E, F) near  $t = t_3$ . By now, three symmetric pairs of vortices appear in the wake, hence the name S-III.

At some point between  $t_3$  and  $t_4$ ,  $U_0$  starts to overtake  $v_c$ . This happens when  $2\pi f_c A \sin(2\pi f_c t + \phi_0) = U_0$ , viz.  $2\pi f_c t + \phi_0 \approx 0.675$ . Consequently, (A, B) and (C, D) convect away from the cylinder in  $-x$  direction and (E, F) moves to the leeward side of the cylinder while  $\Gamma_{E,F}$  increasing. For  $t > t_4$ , the cylinder starts a new cycle, and a new pair (G, H) forms in the same way as (A, B). Induced by the pair (G, H), vortices E and F move towards each other, which explains the formation process of the vortex row along the wake centreline.

The pairs (A, B) and (C, D) shown in Fig. 8 tend to move away from the wake centreline as they are convected downstream. Their trajectory is mainly determined by the relative magnitude of  $\Gamma_{A,B}$  and  $\Gamma_{C,D}$  and their mutual induced velocities. In this case,  $\Gamma_{A,B} \geq \Gamma_{C,D}$  (conjectured from the dye pattern). However, at the same  $A$  and  $f_c$ , when  $U_0$  ( $Re$ ) increases,  $\Gamma_{A,B}$  increases accordingly (since vortices A and B are formed when the cylinder moves upstream, the relative velocity increases), so for  $\Gamma_{G,H}$ . But  $\Gamma_{C,D}$  decreases, which results in  $\Gamma_{A,B} > \Gamma_{C,D}$ . Considering the induced velocity,  $\Gamma_{C,D}$  and  $\Gamma_{E,F}$  tend to pull (A,B) away from the centreline, while  $\Gamma_{G,H}$  brings them inward. Since  $\Gamma_{G,H} \gg \Gamma_{C,D}, (\Gamma_{E,F})$ , (A, B) quickly entrains (C, D) and

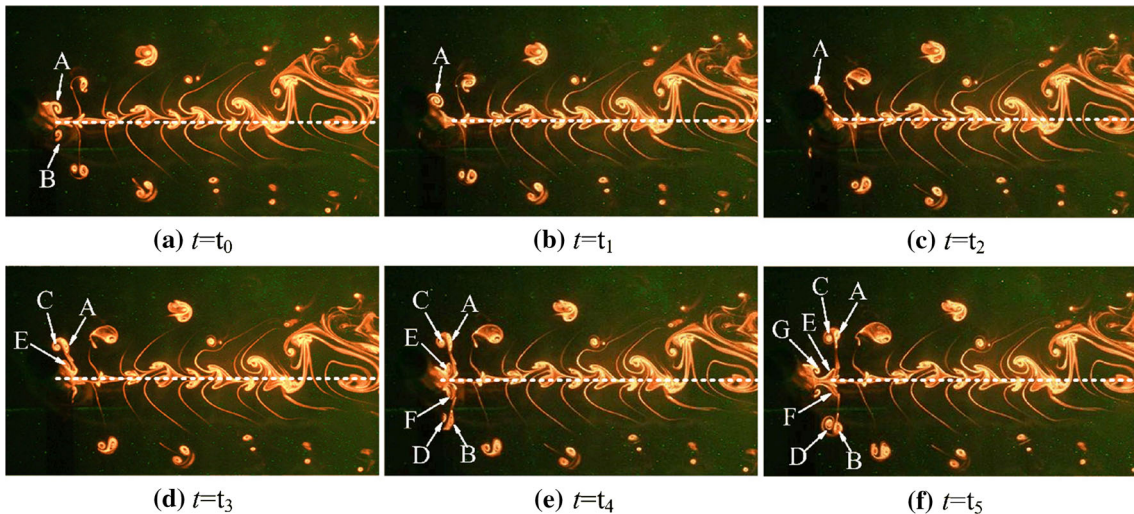


**Fig. 8** Sequential photographs of S-III mode (Type-I) at  $A/d = 0.5$ ,  $f_c/f_s = 3.0$  and  $Re = 360$

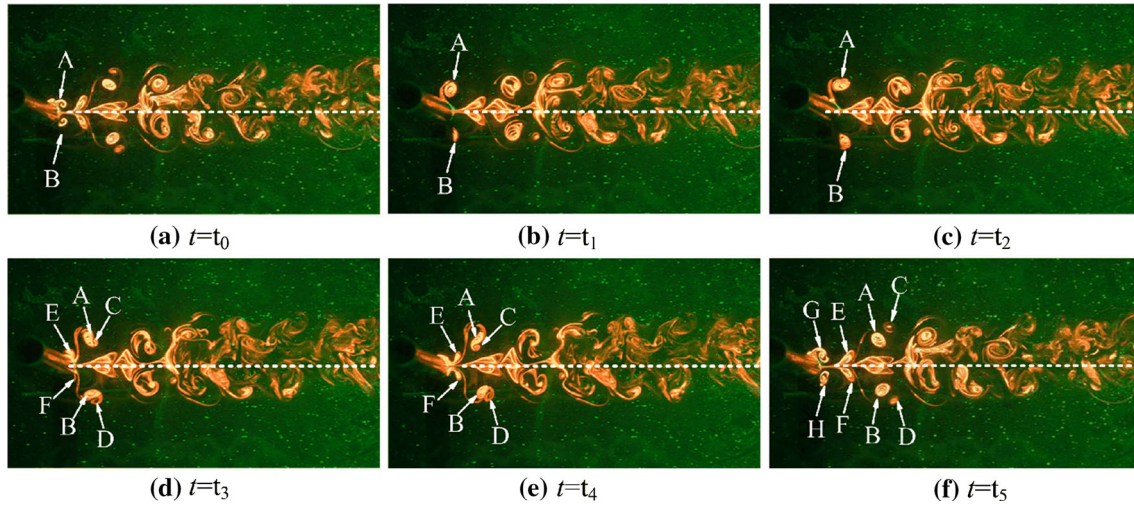


**Fig. 9** Sequential photographs of S-III mode (Type-II) at  $A/d = 0.5$ ,  $f_e/f_s = 3.0$  and  $Re = 430$

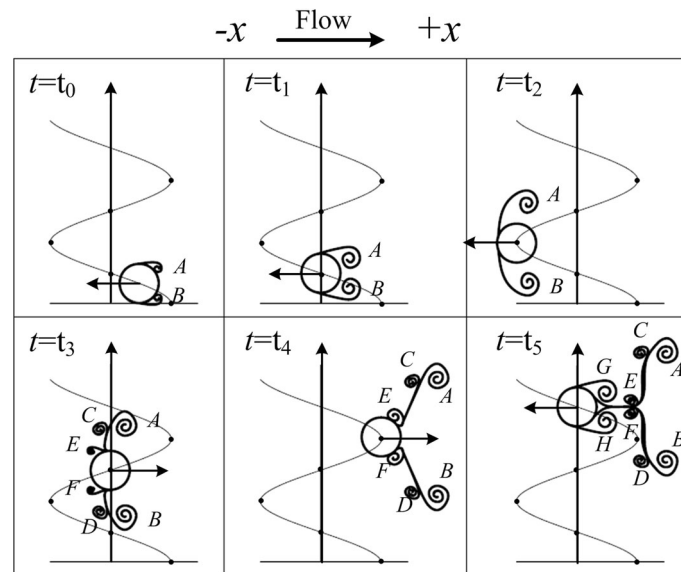


**Fig. 10** Schematic diagram for S-III mode formation process

moves towards the centreline together, as shown in Fig. 9. They then merge with (E, F) to form a symmetric vortex pair of larger size at the centreline.

As expected, similar to submodes Type-I and Type-II of S-III, which are dependent on the motion of the outer pairs (A, B) and (C, D), two sub types can also be observed in S-II mode, according to the same mechanism. This is shown in Appendix 1. As the forcing frequency goes up, wake mode gradually transfers from Type-I to Type-II. Compared to Figs. 8 and 9, in the absence of (E, F), the vortex pair at the wake centreline in S-III Type-II is less distorted, but it also gets unstable and disorganized soon moving downstream.

### 3.3 The mode map

The dependence of modes on  $f_e/f_s$  and  $A/d$  at different  $Re$  is shown in Fig. 11. Each marker represents a testing case studied. It can be seen that at fixed  $Re$  and  $A$ , as the time-invariant  $f_e$  increases from zero, the order of the base mode appearance generally follows a consistent trend, should a mode emerge: Non-Lock-

on  $\rightarrow$  S-I (Type-I)  $\rightarrow$  A-I  $\rightarrow$  A-IV  $\rightarrow$  A-III  $\rightarrow$  S-I (Type-II)  $\rightarrow$  S-II  $\rightarrow$  S-III  $\rightarrow$  C-I/C-II. However, there are some important notes to take. Firstly, according to Xu et al. (2006) and Zhou and Graham (2000), the condition for the emergence of S-II mode, which consists of two pairs of counter-rotating vortices, is written as

$$\Delta Re = \frac{(2\pi f_e A - U_0)d}{\nu} > \frac{u_c d}{\nu} = Re_c \quad (4)$$

Equation (4) is marked in Fig. 11, which essentially ensures that when the cylinder motion is in the same direction as  $U_0$ , the peak motion velocity exceeds  $U_0$  so that the minimum relative velocity results in the rolling-up of +ve vortices (c.f. vortices C and D in Fig. 10). Similarly, the maximum relative velocity between the cylinder and  $U_0$ ,  $|V_{\max}| = 2\pi f_e A + U_0$ , which occurs when the cylinder moves in  $-x$  direction, defines the peak (relative)  $Re$ , denoted as  $Re_p$ , viz.

$$Re_p = \frac{|V_{\max}|d}{\nu} = \frac{2\pi f_e A d}{\nu} + Re \quad (5)$$

It is found that when  $Re_p \geq 1300$ , the shear layer originated from  $|V_{\max}|$  becomes so strong that vortices (c.f. vortices A B in Fig. 10) cannot roll up to a clear structure. The S mode thus becomes the turbulent C-II mode, see Eq. (5) marked in Fig. 11.

Secondly, in order for the S-II mode to emerge, i.e. for +ve vortices to grow to and sustain at a size that can be recognized by the current visualization technique, it is found that a further constraint needs to be applied in addition to Eq. (4). That is, the circulation of the +ve vortices,  $\Gamma_{cp}$ , needs to exceed a threshold. Referring to Fig. 12, it is assumed that the velocity excess  $\Delta u$  will fully roll up to +ve vortices within a cylinder oscillation cycle. Therefore,  $\Gamma_{cp}$  can be estimated as

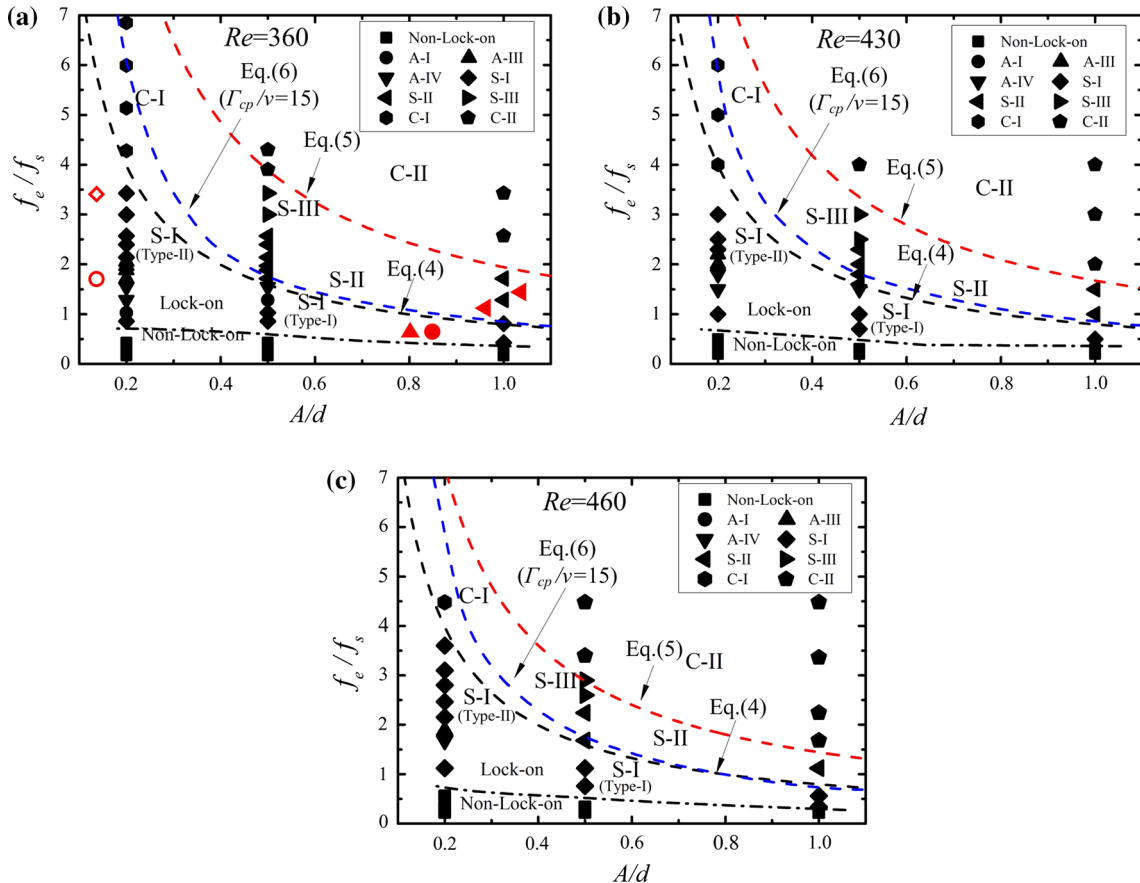


**Fig. 11** Dependence of wake mode on  $A/d$ ,  $f_e/f_s$  and  $Re$ . In a, the red open symbols are taken from Ongoren and Rockwell (1988a),  $Re = 584$ ; the filled red symbols are taken from Konstantinidis and Bouris (2016),  $Re = 180$

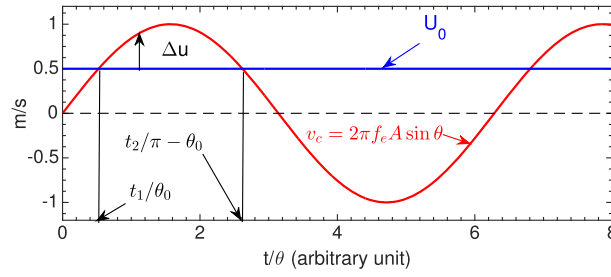


**Fig. 12** Model of +ve vortex formation in S-II mode by  $\Gamma_{cp}$  due to the velocity excess  $\Delta u (= v_c - U_0)$ . Arbitrary  $f_c A$ . The two intersection points of curve  $U_0$  and  $v_c$  are at  $t_1(\theta_0)$  and  $t_2(\pi - \theta)$

$$\Gamma_{cp} \sim \int_0^L \Delta u \, dl = \int_{t_1}^{t_2} \Delta u^2 \, dt = \int_{t_1}^{t_2} (v_c - U_0)^2 \, dt, \quad (6)$$

where  $L$  is the total roll-up length due to  $\Delta u$ ;  $t_1$  and  $t_2$  are indicated in Fig. 12. Changing the integration variable from  $t$  to  $\theta$ , the  $\Gamma_{cp}$  defined  $Re_{cp}$  can then be estimated as

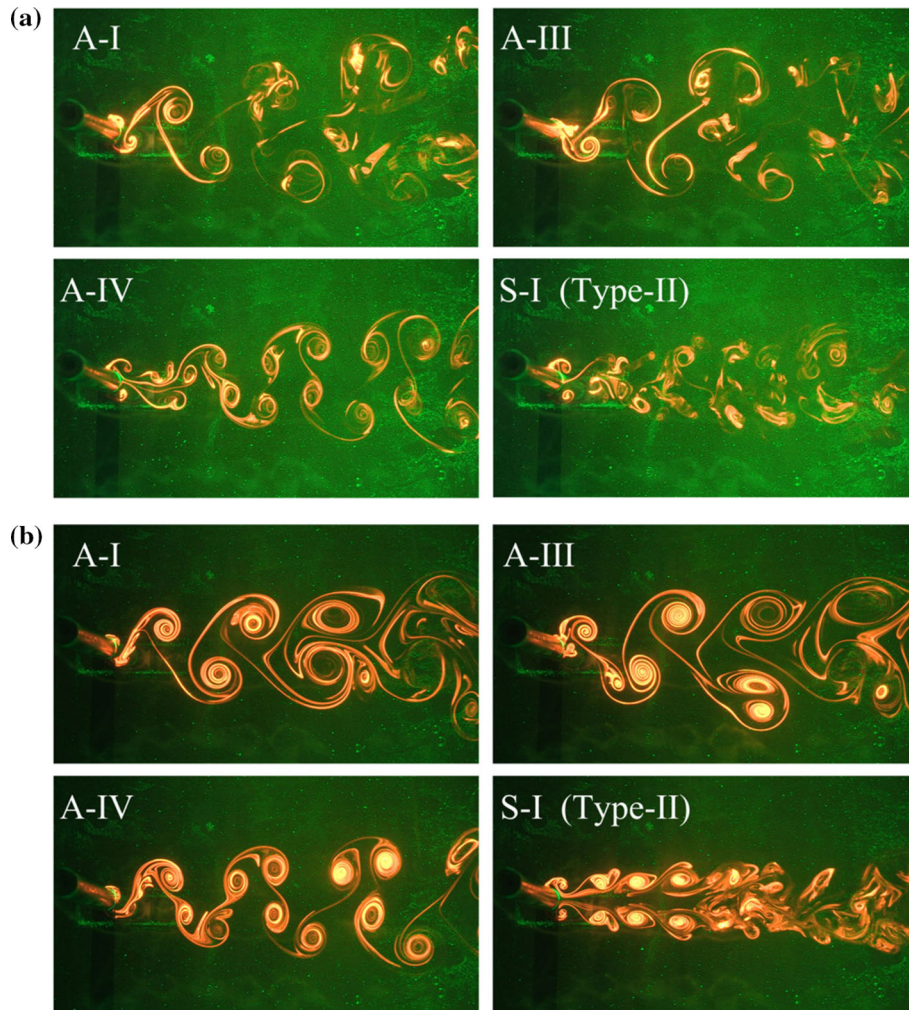


**Fig. 13** Multiple modes observed at **a**  $Re = 360$ ,  $A/d = 0.2$ ,  $f_c/f_s = 2.14$ . **b**  $Re = 430$ ,  $A/d = 0.2$ ,  $f_c/f_s = 2.24$

$$Re_{cp} = \frac{\Gamma_{cp}}{v} \sim \frac{1}{2\pi f_e v} \int_{\theta_0}^{\pi-\theta_0} (2\pi f_e A \sin \theta - U_0)^2 d\theta, \quad (7)$$

where,  $\theta = 2\pi f_e t + \phi_0$  and  $2\pi f_e A \sin \theta_0 = U_0$ . The integration range defines the one over which the cylinder motion exceeds  $U_0$ . Given the estimation of  $\Gamma_{cp}/v$  by Eq. (7), it suggests that for clear S-II mode to emerge, the flow condition needs to satisfy  $\Gamma_{cp}/v \geq 15$ , which is marked in Fig. 11, and at the same time  $Re_p \leq 1300$ .

If the oscillation energy increases to  $\Gamma_{cp}/v \geq 70$  while  $Re_p \leq 1300$ , the relative flow motion to the cylinder in  $+x$  direction will roll up to two +ve vortices and S-III mode form, as described in Sect. 3.2.

Thirdly, when  $\Delta Re < 0$ ,  $2\pi f_e A < U_0$ , the free stream flow will always be in  $+x$  direction with respect to the cylinder and S-II/S-III mode will not occur. Only +ve vortices will form as S-I mode or A modes in the lock-on regime. An interesting observation is that at  $A/d = 0.2$  for  $1 < f_e/f_s < 4$ , S-I modes are separated by a range of A modes. The wake patterns of the S-I mode at  $f_e/f_s \approx 1$  and that at  $f_e/f_s > 2$  (for all three  $Re$ ) appear differently and are denoted as Type-I and Type-II, respectively. These are discussed in Appendix 2.

In addition, not all of the modes can be observed at a fixed oscillation amplitude  $A$ . The higher the  $A$  is, the more modes which will be skipped. For instance, at  $A/d = 0.2$ , most of the modes can be observed, while at  $A/d = 1.0$ , mode A-I  $\rightarrow$  S-III are all skipped. The appearance of mode A-I is very subtle, which can only be seen at an extremely narrow frequency band at  $Re = 360$ ,  $A/d = 0.2$ ,  $f_e/f_s \approx 1$ . The mode distribution is found to be a weak function of  $Re$ , which can also be seen in Fig. 11. However, as  $Re$  increases, the frequency band for both non-lock-on and S-I/S-II/S-III modes shrinks, which agrees with Xu et al. (2006).

More importantly, when  $f_e$  is near the demarcation between A modes and S-I mode (Type-II), unstable transition among neighbouring modes is constantly observed. For example, at  $Re = 360$ ,  $A/d = 0.2$ ,  $f_e/f_s = 2.14$  and  $Re = 430$ ,  $A/d = 0.2$ ,  $f_e/f_s = 2.24$ , observed modes at these fixed conditions are shown in Fig. 13a, b, respectively. The transition among these modes is not in a defined order, but rather in a stochastic manner. It is analogous to ‘mode jump’ observed behind a transversely oscillating cylinder, when the condition is close to the critical curves; see Williamson and Roshko (1988). Since S modes are symmetric about the wake centreline, implying no lift on the cylinder body (see also Leontini et al. 2013), whereas A modes are not, constant lift transitions (jumping) would occur there, which would incur strong fluid force induced structure instability on the cylinder.

Figure 14 presents three instants where mode transition occurs at a fixed forcing condition, which illustrates the transition mechanism. Although Fig. 14 only shows one-way transitions, in experiments, we observed that transitions in the reverse order also take place and equally frequently. It is worth mentioning that in Ongoren and Rockwell (1988b), at  $A/d = 0.2$ ,  $f_e/f_s(\text{A-III}) < f_e/f_s(\text{A-IV})$ , whereas Fig. 11 shows that  $f_e/f_s(\text{A-III}) > f_e/f_s(\text{A-IV})$ . This particular discrepancy is believed to be partly due to different visualization techniques, which influence the rather subjective judgement, and partly due to the unstable nature of the two modes, where transition between them can be caused by very small instability.

#### 4 Wake modes induced by linear ramping $f_e$

Figure 15 presents the mode map as  $f_e$  goes through linear ramp-up, constant and linear ramp-down periods at  $Re = 360$  and various  $k$  values. It corresponds to Fig. 11a at  $A/d = 0.2$ , where the maximum number of modes is observed at constant  $f_e$  conditions. In Fig. 15, each constant  $k$  line is divided into a number of sections within which the mode observed is labelled. It, however, does not mean that a mode switch always occurs abruptly at the labelled mode boundary. As a matter of fact, at which  $f_e$  a mode switch takes place is often difficult to determine objectively by visualization. Therefore, the section boundaries are merely approximations. It is also necessary to point out that similar observations are also made in  $Re = 430$  and 460 cases. Therefore, they are not repeated.

##### 4.1 Mode switches

Compared to the constant  $f_e$  counterpart shown in Fig. 11a, it is necessary to introduce two new labels in Fig. 15. ‘No clear mode’ refers to a period in which the dye streakline pattern is highly turbulent and hardly any mode can be identified. Figure 16 displays an example of such mode as wake pattern changes from S-I (Type-I) to A-III. Evidently, the streakline is highly blurry and the pattern is very difficult, if possible, to categorize to a definite mode. Note also the patchy appearance of the dye blobs in this mode, which is

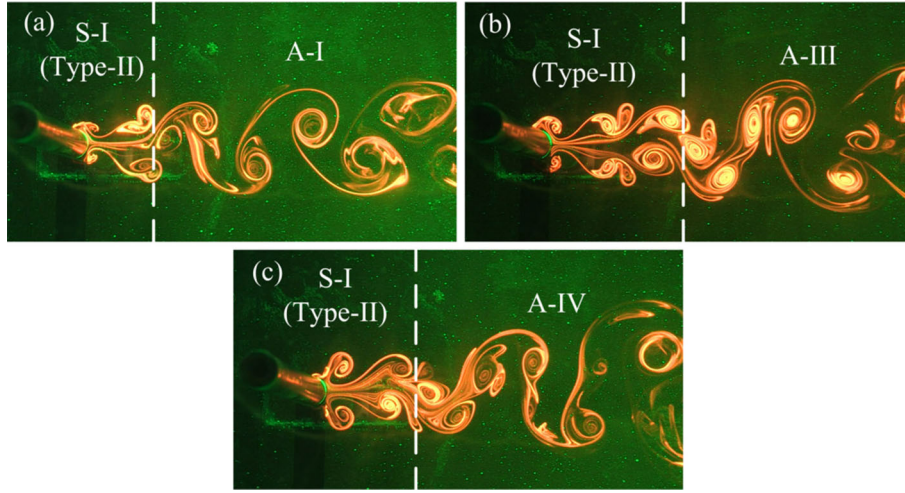


**Fig. 14** Mode transition process at  $A/d = 0.2$  and **a**  $f_e/f_s = 2.14$ ,  $Re = 360$ . **b**, **c**  $f_e/f_s = 2.24$ ,  $Re = 430$

appreciably different to the C-II mode. The number of oscillation cycles  $N$  spent in this period varied significantly at different  $k$ , which can be calculated as

$$N = \int_{f_{e1}}^{f_{e2}} \frac{f_e}{k} df_e = \frac{1}{2k} f_s^2 \left[ \left( \frac{f_e}{f_s} \right)_2^2 - \left( \frac{f_e}{f_s} \right)_1^2 \right], \quad (8)$$

where the subscripts 1 and 2 denote the start and the end of the switching period, respectively. As  $k$  increases, both  $N$  and  $N_{rp}$  (representing the number of cycles of the *entire* ramp-up period) decreases, but the proportion of time spent in the switching period with respect to  $N_{rp}$  increases dramatically. For instance,  $N$  on the  $k = 0.44s^{-2}$  line is about 2.1, which spans over 50 % of  $N_{rp}$ . Also note that according to Eq. (8), at the highest  $k = \pm 0.44s^{-2}$ , it only takes about 4 complete cycles to ramp-up/-down to/from the largest forcing frequency  $f_e = 3.5f_s$ .

Mode ‘slow switch’ refers to the  $f_e$  range over which wake pattern typically displays organized unidirectional switches from one mode to another, with the feature being unidirectional ‘slow switches’ with respect to ‘jump switches’, which will be discussed later. Figure 17 presents the mode switch from S-I (Type-II) to A-IV during  $2.1 \leq f_e/f_s \leq 2.2$  on  $k = -0.02s^{-2}$  line. The switch is in an organized manner and one direction, which is different from mode transition in fixed  $f_e$  conditions where mode change is bidirectional. A possible explanation for the difference is that the downstream part, which contains stronger vortices originated from more energetic higher frequency oscillation, has some influence to the near wake (via induced velocities) which is being formed by less energetic oscillation. It is not the case for  $k = 0$  scenario, as the near field and the far field are equally energetic and the bidirectional transition is probably owing to modal instability. Any mode switch between two modes which are separated by such a mode switch takes typically  $N = 4-7$  cylinder oscillation cycles to complete according to Eq. (8), e.g. S-I (Type-II)

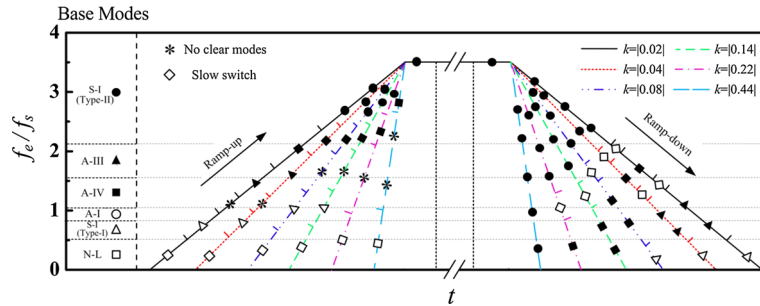


**Fig. 15** Mode map at  $Re = 360$ ,  $A/d = 0.2$ ,  $f_e = f_0 + kt$ , where  $f_0 = 0$  and  $k$  values are marked on each line. The constant  $f_e$  period lasts for 30 s. The mode conditions at constant  $f_e$  ( $k = 0$ , the base modes) are duplicated from Fig. 11a and displayed along the y-axis

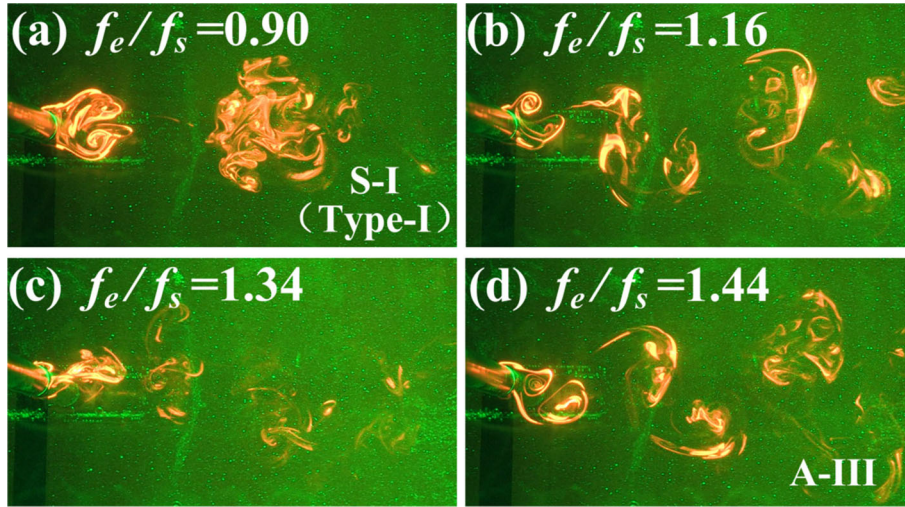


**Fig. 16** No clear mode period from mode S-I (Type-I) to A-III at  $Re = 360$ ,  $A/d = 0.2$ ,  $k = 0.02s^{-2}$

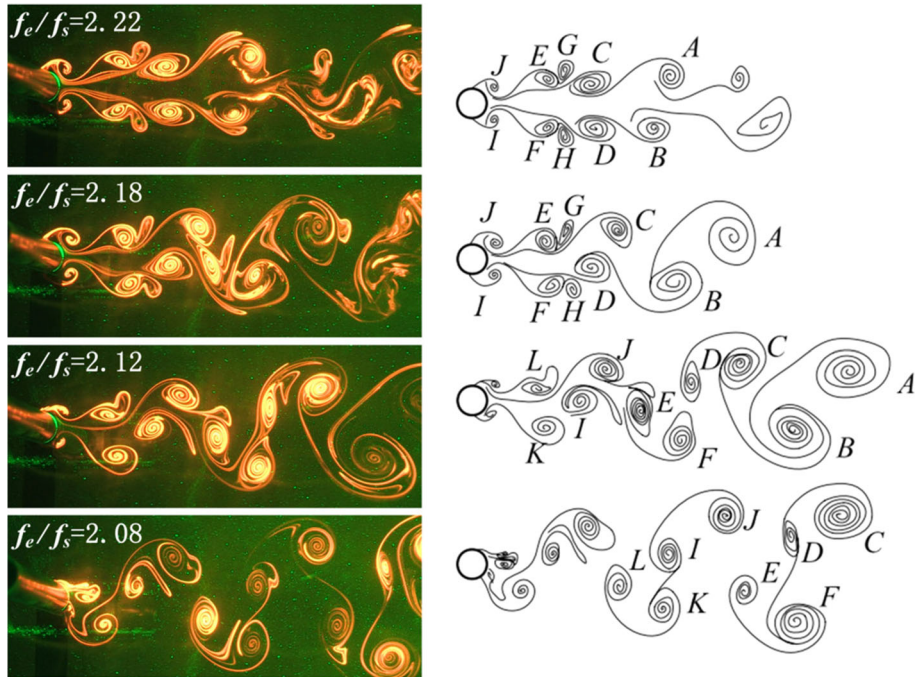
→ A-IV → A-III on  $k = -0.02s^{-2}$  line. Another example of a similar switch S-II → A-IV is illustrated in Fig. 18, where  $A/d = 0.5$ .

Figure 17 shows that as forcing frequency approaches  $f_e/f_s = 2.22$ , the downstream vortex pair (A, B), under the influence of the slowed down  $f_e$  on the cylinder, starts to deform from the symmetric arrangement at  $x \approx 5d$ . As  $f_e$  continues decreasing, deformation propagates upstream. For instance, at  $f_e/f_s = 2.18$ , vortex pair (I, J), immediately shed from the cylinder starts to depart from a symmetric arrangement. Soon after, secondary vortices G(K) and H(L) are unable to be generated when the cylinder moves upstream, which in turn causes the counter-rotating vortices (C, D) and (E, F) downstream starting to move away from the centreline. As these vortex pairs convect downstream, the deformation becomes severer and eventually the entire wake displays A-IV mode by  $f_e/f_s \approx 2.0$ . Figure 18 shows a similar scenario, where mode switch from S-II to A-IV starts from a downstream region and propagates upstream.

Figure 19 depicts the mechanism of mode switch from A-IV to A-III, which is the second switching period along  $k = -0.02s^{-2}$  line. It shows that mode switch also starts from downstream, viz. vortex pairs (A, B) and (C, D). The crucial moment of this particular mode switch is the combination of the vortices of the same rotation sense J and K at  $f_e/f_s = 1.32$ . In a similar manner, vortex B was attached to and fused by C. Soon after, the downstream vortex F dies in the same way as B, under the influence of the upstream event. It leads to one vortex loss and hence the switch from A-IV to A-III. As  $f_e$  keeps dropping, such vortex combination is no longer seen in the wake and the wake turns to the resultant A-III mode. The switch is thus completed.

Mode switches during frequency ramping-down ( $k < 0$ ) all go through such slow switch exclusively. On the contrary, during frequency ramping-up period ( $k > 0$ ), except mode switches from non-lock-on/S-I (Type-I) to A-IV/A-III, which is of no clear mode type, all the other switches are rather abrupt, namely ‘jump switch’.

Figures 20 and 21 depict the mode switch from A-IV and A-III to S-I (Type-II), respectively. Similar to slow switch, jump switch is also unidirectional. Nevertheless, the key differences to the former are that firstly, the switch is initiated on the cylinder rather than in the downstream wake, and secondly, as the current mode switches to a new one, the downstream vortex arrangement is not affected by the upstream one. For instance, the pattern of vortex pair (A, B) in Fig. 20 and the arrangement of vortices (A–F) in Fig. 21, as they convect downstream, remain unchanged. As such, there is a location somewhere in the wake with a modal jump across, as illustrated by  $f_e/f_s = 2.44$  in Fig. 20 at E and  $f_e/f_s = 2.72$  in Fig. 21, at K. Other noticeable features related to such switch include the vortex combination of B and C in Fig. 20, combination of H and G, as well as the reforming of vortex pair (J, H) in Fig. 21. Such a mode jump in the wake is analogues to the one reported in Williamson and Roshko (1988) behind a transversely forcing cylinder when mode 2S switch to mode 2P, as the oscillation wavelength decreases, which is equivalent to frequency increment ( $k > 0$ ) in our experiments.



**Fig. 17** Slow switch from S-I (Type-II) mode to A-IV mode at  $Re = 360$ ,  $A / d = 0.2$ ,  $k = -0.02s^{-2}$

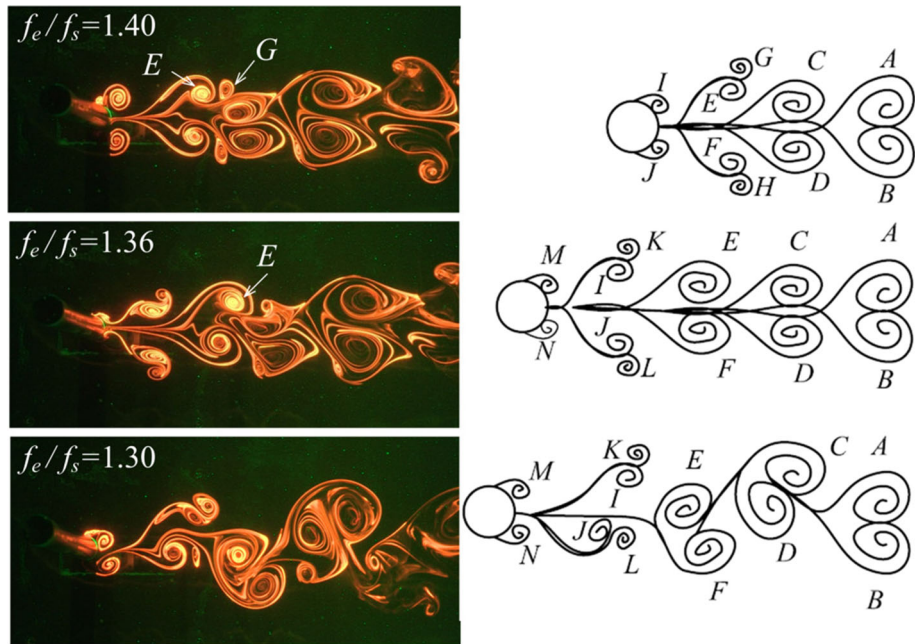


**Fig. 18** Slow transition from S-II mode to A-IV mode at  $Re = 360$ ,  $A / d = 0.5$ ,  $k = -0.02s^{-2}$

#### 4.2 Mode skip and hysteresis

Some other noticeable differences can be observed when we compare the modes appeared in frequency ramping durations to the constant frequency counterparts. Firstly, comparing the modes in  $k = +0.02s^{-2}$  process in Fig. 15 and the corresponding ones of constant  $f_e$ , viz. the base modes in Fig. 11a, we may notice a modal order reversal, i.e. A-III  $\rightarrow$  A-IV during ramping case whereas  $f_e(\text{A-IV}) < f_e(\text{A-III})$  at constant  $f_e$ . This might be owing to the fact that the difference between the two modes is very subtle and both are



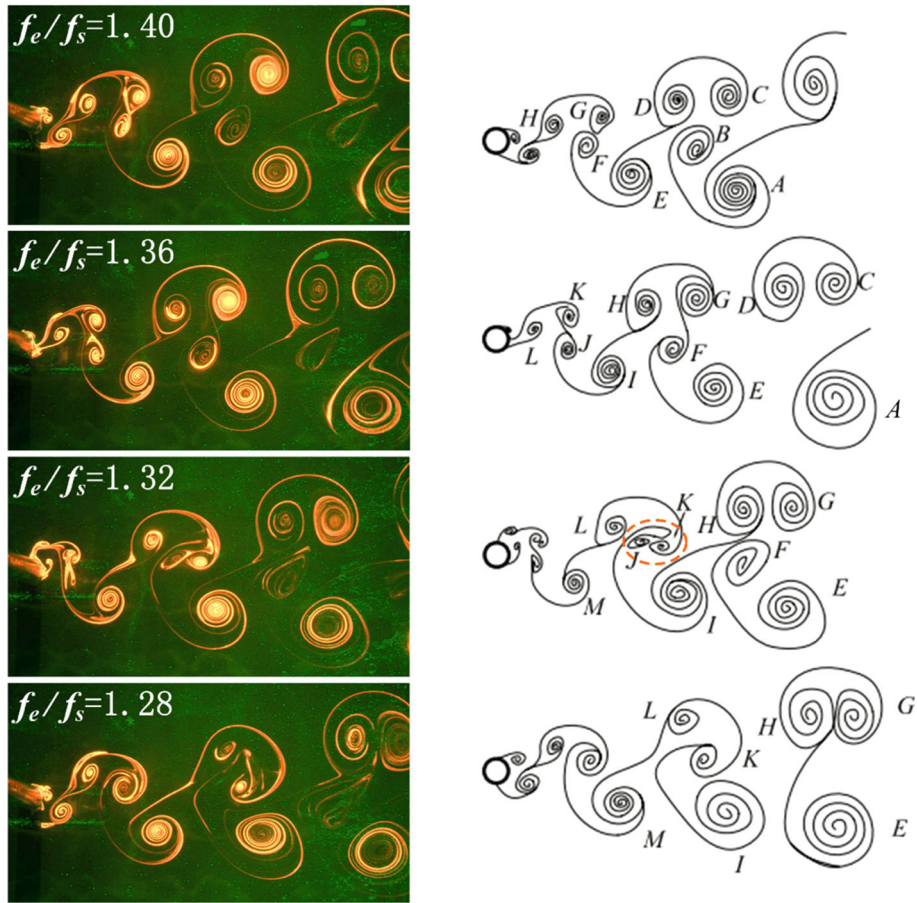


**Fig. 19** Slow switch from A-IV mode to A-III mode at  $Re=360$ ,  $A / d=0.2$ ,  $k = -0.02s^{-2}$

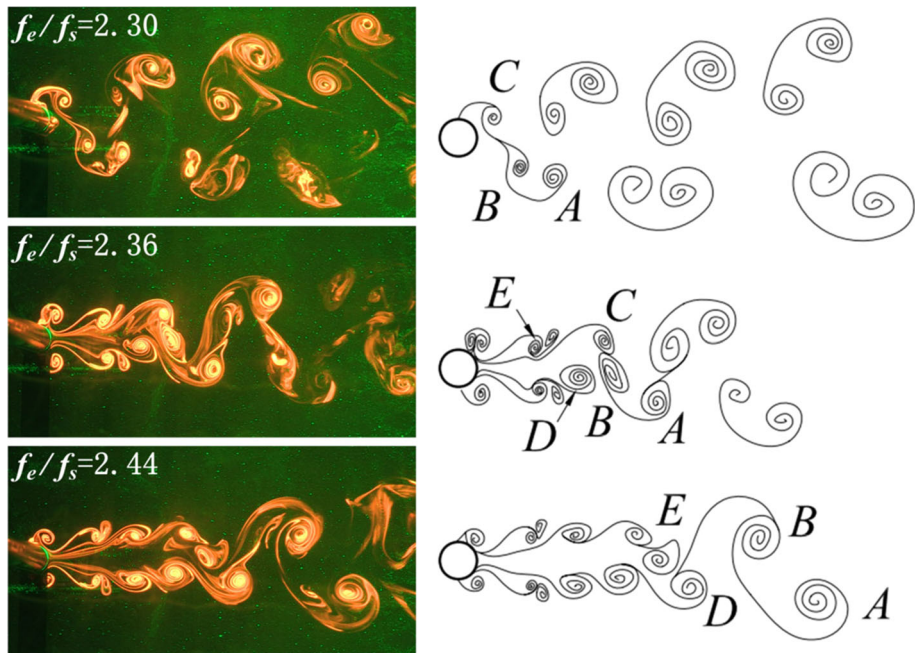


**Fig. 20** Jump switch from A-IV mode to S-I (Type-II) mode at  $Re = 360$ ,  $A / d = 0.2$ ,  $k = +0.02s^{-2}$

unstable (sensitive to frequency change) by nature. It is evident in Fig. 11a that multiple modes exist in a narrow frequency band  $1 \leq f_e/f_s \leq 2$ . In this respect, mode S-II and C-I are much more stable.

Secondly, fewer modes are identified when the forcing frequency changes quickly, i.e. as  $|k|$  increases, some modes are skipped. For instance in Fig. 15, as  $k$  increases from  $+0.04s^{-2}$  to  $+0.08s^{-2}$ , mode A-III is skipped while A-IV can still be observed, even though its frequency band becomes narrower, which suggests that mode A-IV is more stable. As  $k$  is set at the maximum ramping rate  $+0.44s^{-2}$ , only one lock-on mode A-IV can be seen. Similar observations can be made for  $k < 0$  cases. The number of modes that can be identified dropped from 4 at  $k = -0.02s^{-2}$  to 1 (only S-II) at  $k = -0.04s^{-2}$ . Note that at  $k = \pm 0.44s^{-2}$ , the total number of oscillation cycles spent in the ramping period is only  $N = 4$  according to Eq. 8, which leaves no time for more modes to emerge.

Thirdly, during the ramp-up period, the occurrence of S-I (Type-II) and S-II modes is clearly delayed in terms of the occurrence  $f_e$  compared to the base modes, as indicated by the horizontal grid lines. Such a delay becomes more significant as  $k$  increases. Similarly, the corresponding  $f_e$  for the occurrence of mode A-III (if possible), A-IV and S-I (Type-II) or S-II also gets delayed, while the frequency bands for the non-lock-on mode and no clear mode expand. During the ramp-down period, on the other hand, the terminal  $f_e$  for S-I (Type-II) mode range is postponed compared to the base modes, especially as  $|k|$  increases. Also, the corresponding  $f_e$  for the occurrence of slow switch and A-IV mode is also gradually deferred, with the frequency band of slow switch enlarged marginally.

Consequently, the most striking feature of Fig. 15 perhaps is the asymmetry of the modal distribution during the ramp-up and ramp-down periods. Not only the modes themselves, but also their occurrence  $f_e$  exhibit asymmetry. Although the mode divisions in Fig. 15 along a constant  $k$  line are approximations, the hysteretic effect is discernable, as shown by the marked horizontal grid lines. As discussed above, hysteresis also exists between the ramp-up and the base modes. Figure 22 presents an example of hysteresis for mode switches from A-IV to S-I (Type-II).

For the base modes, as shown in Fig. 15a, mode A-III appears in between A-IV and S-I (Type-II); mode S-I (Type-II) starts at  $f_e/f_s \approx 2.14$ . The mode switch from A-IV to S-I (Type-II) during frequency ramp-up ( $k = +0.02s^{-2}$ ), which occurs at  $f_e/f_s \approx 2.3$  along a vertical line, indicates a jump switch. The switch is deferred to a higher  $f_e$  compared to the base mode switch. As frequency ramps down at  $k = -0.02s^{-2}$ , it takes a range of  $2.03 < f_e/f_s < 2.14$ , for the mode switch from S-I (Type-II) to A-IV to complete, which denotes a slow switch. Therefore, hysteresis for mode S-I (Type-II) is approximately

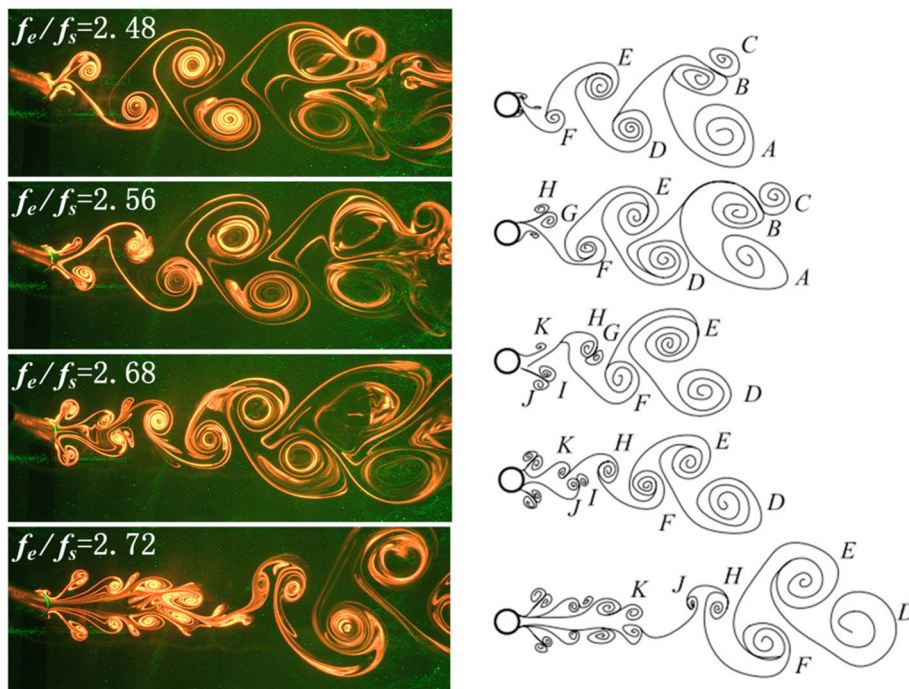
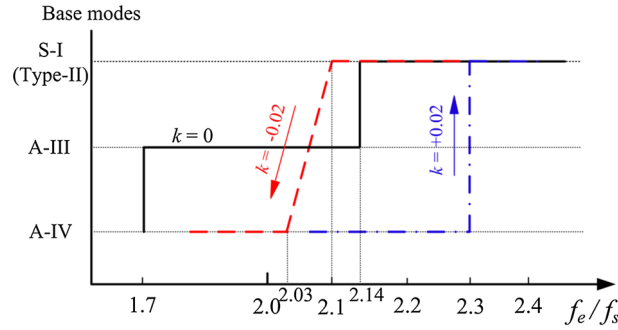
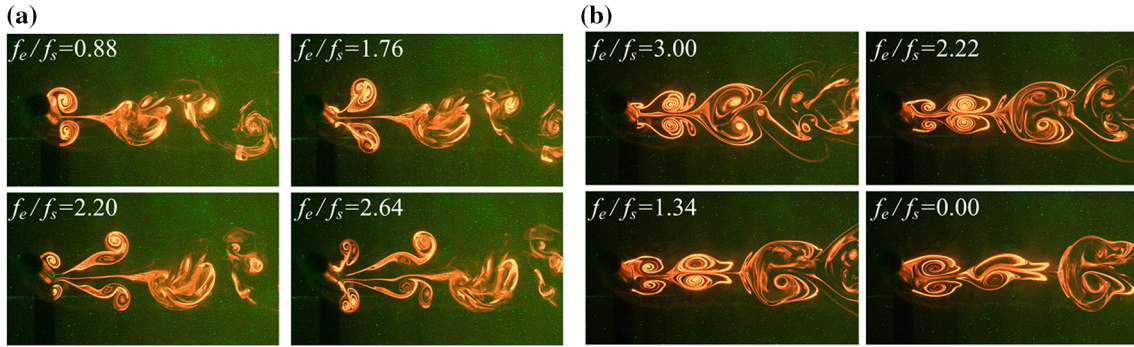


Fig. 21 Jump switch from A-III mode to S-I (Type-II) mode at  $Re = 430$ ,  $A/d = 0.2$ ,  $k = +0.04s^{-2}$



**Fig. 22** Mode hysteresis between A-IV to S-I(Type-II) at  $Re = 360$ ,  $A / d = 0.2$ ,  $k = \pm 0.02s^{-2}$  and base modes ( $k = 0$ )



**Fig. 23** The large-scale symmetric structure appears when  $f_e$  goes through linear ramp-up or down rapidly. **a**  $Re = 360$ ,  $A / d = 0.2$ ,  $k = +0.44s^{-2}$ , **b**  $Re = 360$ ,  $A / d = 0.2$ ,  $k = -0.44s^{-2}$

$$\Delta f_e^1 = f_e(k = +0.02) - f_e(k = 0) \approx 0.16f_s \quad \text{and} \quad \Delta f_e^2 = f_e(k = 0) - f_e(k = -0.02) \approx 0.04f_s, \quad \text{hence} \\ \Delta f_e = f_e(k = +0.02) - f_e(k = -0.02) \approx 0.2f_s.$$

Hysteresis  $\Delta f_e$  generally increases for other modes at higher  $k$ , which can be inferred by Fig. 15. At the largest  $|k| = 0.44s^{-2}$ , mode S-I (Type-II) is not seen in the ramp-up period until the  $k = 0$  at the plateau, while mode switch from S-I (Type-II) does not occur in the ramp-down period. Hysteresis can thus be considered as at maximum degree, since  $\Delta f_e$  is not defined. Figure 23 presents the large-scale symmetric structure appears when  $f_e$  goes through linear ramp-up or down rapidly.

## 5 Conclusion

In this paper, the wake modes behind a circular cylinder in streamwisely oscillating motion are studied at higher forcing frequencies under  $Re = 360$ – $460$ , using LIF flow visualization. The forcing frequency  $f_e/f_s$  ranges from 0 to 6.85 and the amplitude  $A / d (= 0.2, 0.5, 1.0)$ . Both time-invariant and linear ramping  $f_e$  are investigated. The following conclusions can be drawn:

(1) Three rarely reported modes (C-I, C-II and S-III) are identified at higher  $A$  and/or  $f_e$  ranges than those applied in previous studies. The appearance of the lock-on modes at a fixed  $A$  generally follows the order S-I (Type-I)  $\rightarrow$  A modes  $\rightarrow$  S-I (Type-II)  $\rightarrow$  S-II/S-III  $\rightarrow$  C modes, as the time-invariant  $f_e$  increases. When  $f_e$  is close to the demarcation frequency between A modes and S-I (Type-II) mode, i.e. at  $A / d = 0.2$  and  $2.14 \leq f_e/f_s \leq 2.24$  depending on  $Re$ , unsteady bidirectional mode transitions are observed, where multiple modes coexist and transfer back and forth from one to another. At fixed  $f_e$ , the additional constraint for the occurrence of S-II, C-I and C-II modes are also modelled from which, envelope lines for these modes are marked on the mode map based on empirical parameters.

(2) More new observations can be made as the oscillation frequency  $f_e$  undergoes linear ramping. As the magnitude of the ramping rate  $|k|$  increases, more modes are skipped compared to the base modes ( $k = 0$ ) for the same  $f_e$  range. Also, the mode distribution is found to be asymmetric between ramp-up ( $k > 0$ ) and ramp-down ( $k < 0$ ) ranges, which is a typical hysteretic effect. By and large,  $f_e$  for a certain mode to occur is deferred in  $k > 0$  compared to  $k = 0$  cases, while it is further postponed during the  $k < 0$  range. The degree of

delay is in line with  $|k|$ , i.e. the larger the ramping rate, the larger the hysteresis effect. At the largest  $|k|=0.44s^{-2}$ , which is the highest ramping rate tested, except the base mode S-II, only A-IV appears for a small  $f_e$  range during ramp-up, while no other modes can be seen during ramp-down.

(3) Mode changes during frequency ramping all obey unidirectional switches. However, the switch processes are different for ramp-up and ramp-down durations. During  $k < 0$ , when S-II or S-I (Type-II) mode switch to A-IV mode, or A-IV to A-III, the flow structure in downstream is affected by the upstream and the entire wake flow eventually switched, which is a slow switch. In contrast, during  $k > 0$ , a clear and abrupt switch can be observed in the wake when A-IV or A-III switch to S-I (Type-II) modes. This type of switch is named jump switch.

**Acknowledgements** S.J. Xu wishes to acknowledge the support from NSFC through Grants 11772173, 91752203 and 11472158. L. Gan would like to thank the support from Durham University International Engagement Grant.

**Open Access** This article is distributed under the terms of the Creative Commons Attribution 4.0 International License (<http://creativecommons.org/licenses/by/4.0/>), which permits unrestricted use, distribution, and reproduction in any medium, provided you give appropriate credit to the original author(s) and the source, provide a link to the Creative Commons license, and indicate if changes were made.

## Appendixes

### Appendix 1: The submode transition of S-II mode

Figure 24 shows the submode transition of S-II mode observed in the present study. According to Eqs. (5) and (9), S-II mode will occur when  $Re_p \geq 1300$  and  $\Gamma_{cp}/\nu \geq 15$ . Generally speaking at  $Re = 360$ , if  $(A/d)/(f_e/f_s) < 0.85$ , the wake exhibits large-scale vortex pairs emerging along the wake centreline, which

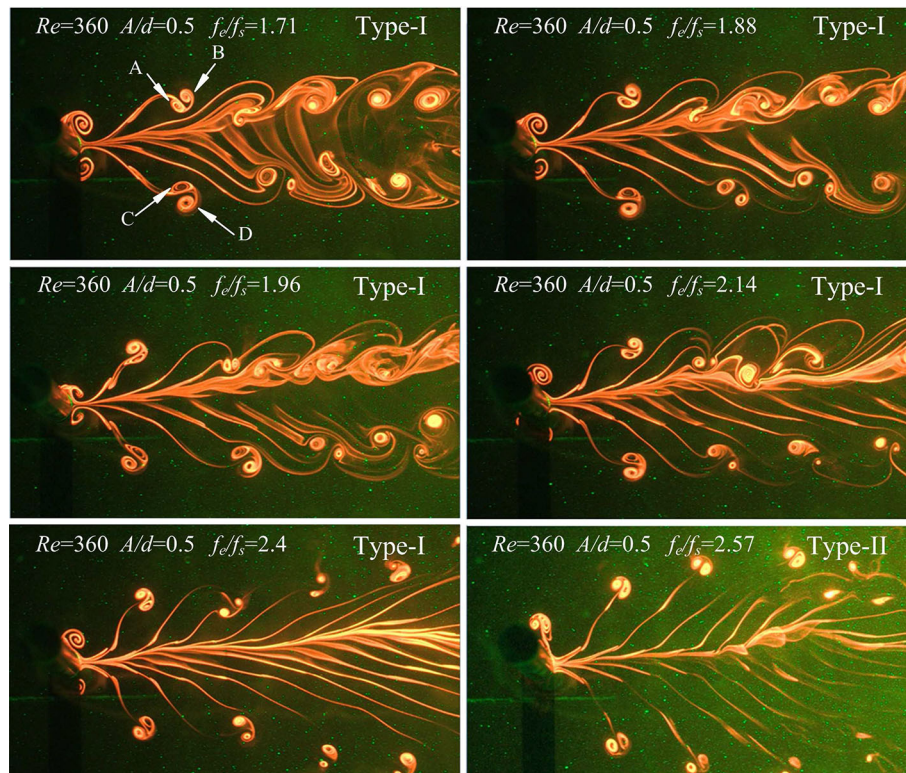


**Fig. 24** The S-II wake submodes observed in the current study

are resulted from the two counter-rotating pairs (A,B) and (C,D) moving towards the wake centreline. This is denoted as Type-I. As  $(A/d)/(f_e/f_s)$  increase, (A,B) and (C,D) gradually move towards the outer flow, forming two rows of counter-rotating vortices, denoted as Type-II. The transition from Type-I to II is not an abrupt process.

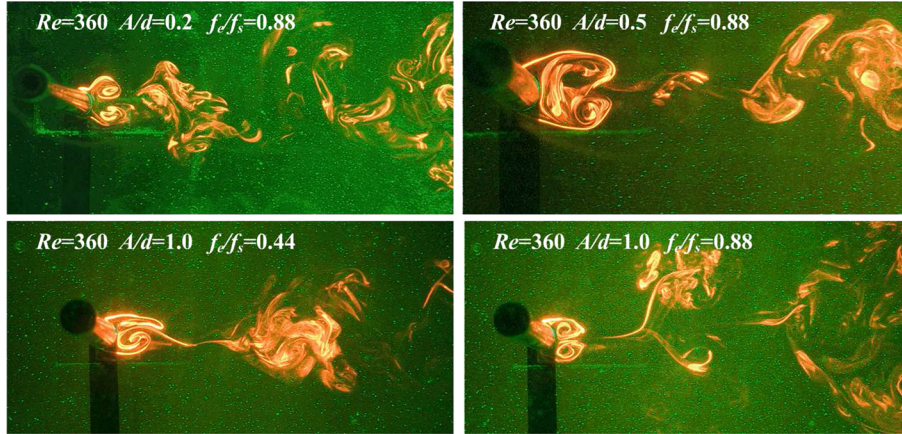
## Appendix 2: The submode transition of S-I mode

Regardless of  $Re$  range tested in the present work, when the flow condition reaches the lock-on regime but  $Re_c \leq 5$ , the symmetric S-I mode occurs. As mentioned in Sect. 3.3, two types of S-I modes are observed, namely the submode Type-I and Type-II, which are separated by a range of anti-symmetric A modes. These are presented in Fig. 25. In Type-I submode, the wake displays a patchy pair of large symmetric vortices, which quickly turns to turbulent. In Type-II, a long row of symmetric vortex pairs survives until the end of the FOV, when they become unstable. To explain the formation process between the two distinctive submodes, we may follow the idea behind Eq. (9), i.e. the circulation  $\Gamma_s$  from the relative motion of  $U_0$  and cylinder surface. For S-I mode,  $U_0 > 2\pi f_e A$  all the time, so  $\Gamma_s$  defined  $Re_s$  for one cycle of cylinder oscillation can be written as:

$$Re_s = \frac{\Gamma_s}{\nu} \sim \frac{1}{2\pi f_e \nu} \int_0^{2\pi} [U_0 - 2\pi f_e A \sin \theta]^2 d\theta \quad (9)$$

Defining  $\gamma = Re_s/Re$ , it can be shown that

Type-I:



Type-II:

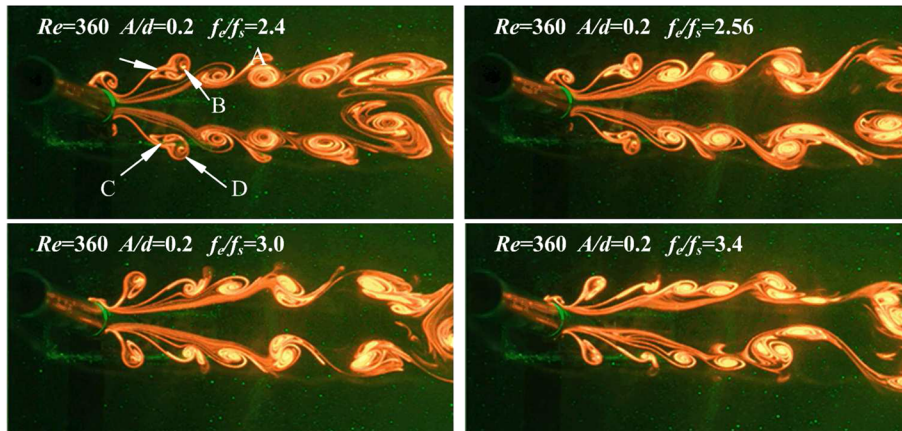
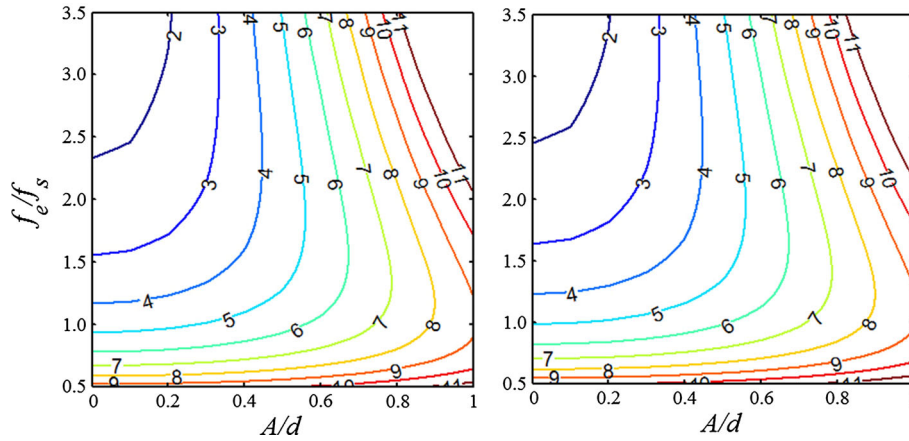
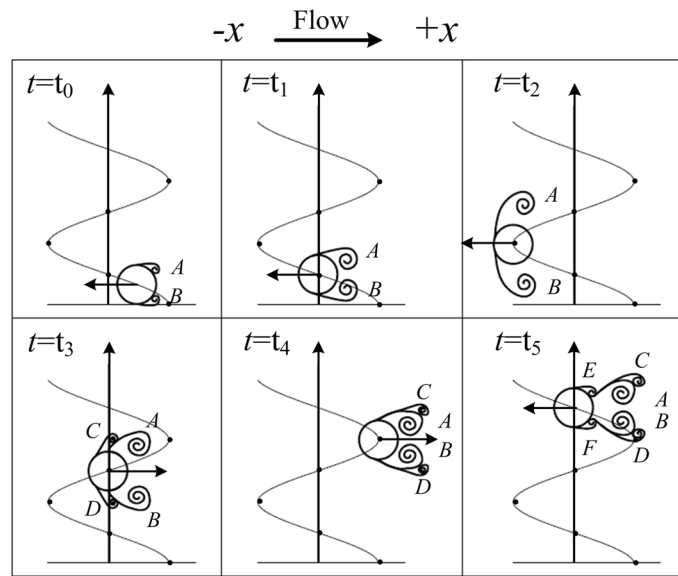


Fig. 25 The S-I wake submodes observed in the current study



**Fig. 26** The dependence of  $\gamma$  on ( $A / d$ ) and ( $f_e/f_s$ ). **a**  $Re = 360$ , **b**  $Re = 460$ ,  $Re = 430$  is almost identical to **(b)**



**Fig. 27** Schematic diagram for S-I (Type-II) mode formation process

$$\gamma = St^{-1} \left(\frac{f_e}{f_s}\right)^{-1} + 2\pi St \left(\frac{f_e}{f_s}\right) \left(\frac{A}{d}\right)^2 \tag{10}$$

The dependence of  $\gamma$  on ( $A / d$ ) and ( $f_e/f_s$ ) is presented in Fig. 26. Therefore, it can be deduced that on the one hand, if  $\gamma \geq 5$ , the energy ( $\Gamma_s$ ) of the vortex formed over a cycle will be too large compared to the free stream energy and they appear very turbulent. The flow field quickly goes patchy. So Type-I is formed. On the other hand, when  $\gamma \leq 2$  the relative energy of the vortices is sufficiently low for them to maintain they structure and hence Type-II emerged. In between,  $2 \leq \gamma \leq 5$  the vortices formed are not so energetic but unstable, so the alternative anti-symmetric A mode forms. When the vortices form on the cylinder surface in Type-II, the shear layer will not roll up into a single pair. Instead, two pairs of the same rotation sense will appear, which is schematically explained in Fig. 27. Due to the time-varying relative velocity  $U_0 - 2\pi f_e A \sin(2\pi f_e t + \phi_0)$ , two pairs (A, B) and (C, D) form, with  $\Gamma_{A,B} > \Gamma_{C,D}$  typically.

## References

- Cetiner O, Rockwell D (2001) Streamwise oscillations of a cylinder in steady current. Part 2. Free-surface effects on vortex formation and loading. *J Fluid Mech* 427:29–59
- Couder Y, Basdevant C (1986) Experimental and numerical study of vortex couples in two-dimensional flows. *J Fluid Mech* 173:225–251
- Detemple-Laake E, Eckelmann H (1989) Phenomenology of Karman vortex streets in oscillatory flow. *Exp Fluids* 7:217
- Griffin OM, Ramberg SE (1976) Vortex shedding from a cylinder vibrating in line with an incident uniform flow. *J Fluid Mech* 75(2):257–271
- Konstantinidis E (2014) On the response and wake modes of a cylinder undergoing streamwise vortex-induced vibration. *J Fluids Struct* 45:256–262
- Konstantinidis E, Balabani S (2007) Symmetric vortex shedding in the near wake of a circular cylinder due to streamwise perturbations. *J Fluids Struct* 23(7):1047–1063
- Konstantinidis E, Bouris D (2016) Vortex synchronization in the cylinder wake due to harmonic and non-harmonic perturbations. *J Fluid Mech* 804:248–277
- Leontini JS, Jacono DL, Thompson MC (2013) Wake states and frequency selection of a streamwise oscillating cylinder. *J Fluid Mech* 730:162–192
- Naudascher E (1987) Flow-induced streamwise vibrations of structures. *J Fluids Struct* 1(3):265–298
- Nishihara T, Kaneko S, Watanabe T (2005) Characteristics of fluid dynamic forces acting on a circular cylinder oscillated in the streamwise direction and its wake patterns. *J Fluids Struct* 20:505
- Ongoren A, Rockwell D (1988a) Flow structure from an oscillating cylinder Part 1. Mechanisms of phase shift and recovery in the near wake. *J Fluid Mech* 191:197–223
- Ongoren A, Rockwell D (1988b) Flow structure from an oscillating cylinder Part 2. Mode competition in the near wake. *J Fluid Mech* 191:225–245
- Sarpkaya T (2004) A critical review of the intrinsic nature of vortex-induced vibrations. *J Fluids Struct* 19(4):389–447
- Sarpkaya T, Putzig C, Gordon D, Wang X, Dalton C (1992) Vortex trajectories around a circular cylinder in oscillatory plus mean flow. *J Offshore Mech Arct Eng* 114(4):291–298
- Sieber M, Paschereit CO, Oberleithner K (2016) Spectral proper orthogonal decomposition. *J Fluid Mech* 792:798–828
- Song L, Song F (2003) Regimes of vortex shedding from an in-line oscillating circular cylinder in the uniform flow. *Acta Mech Sin* 19(2):118
- Tanida Y, Okajima A, Watanabe Y (1973) Stability of a circular cylinder oscillating in uniform flow or in a wake. *J Fluid Mech* 61(4):769–784
- Williamson CHK, Govardhan R (2004) Vortex-induced vibrations. *Annu Rev Fluid Mech* 36:413–455
- Williamson CH, Roshko A (1988) Vortex formation in the wake of an oscillating cylinder. *J Fluids Struct* 2(4):355–381
- Xu S (2003) Fluid-structure interactions of an oscillating cylinder in cross flow in the presence of a neighbouring cylinder. Doctoral dissertation, The Hong Kong Polytechnic University
- Xu SJ, Zhou Y, Wang MH (2006) A symmetric binary-vortex street behind a longitudinally oscillating cylinder. *J Fluids Struct* 556:27–43
- Yufei Z, Zhixiang X, Song F (2007) Analysis of vortex shedding modes of an in-line oscillating circular cylinder in a uniform flow. *Acta Mech Sin Chin Ed* 39(3):408
- Zhang Q, Liu Y, Wang S (2014) The identification of coherent structures using proper orthogonal decomposition and dynamic mode decomposition. *J Fluids Struct* 49:53–72
- Zhou CY, Graham JMR (2000) A numerical study of cylinders in waves and currents. *J Fluids Struct* 14(3):403–428